arXiv:1408.4172v2 [cond-mat.supr-con] 3 Sep 2014

Tunneling Conductance and Spin Transport in Clean Ferromagnet-Ferromagnet-Superconductor Heterostructures

Chien-Te Wu,[1,*] Oriol T. Valls,[1,†] and Klaus Halterman[2,‡]

[1]*School of Physics and Astronomy, University of Minnesota, Minneapolis, Minnesota 55455*
[2]*Michelson Lab, Physics Division, Naval Air Warfare Center, China Lake, California 93555*

(Dated: September 4, 2014)

We present a transfer matrix approach that combines the Blonder-Tinkham-Klapwijk (BTK) formalism and self-consistent solutions to the Bogolibuov-de Gennes (BdG) equations and use it to study the tunneling conductance and spin transport in ferromagnet (F)-superconductor (S) trilayers (F_1F_2S) as functions of bias voltage. The self-consistency ensures that the spin and charge conservation laws are properly satisfied. We consider forward and angularly averaged conductances over a broad range of the strength of the exchange fields and F thicknesses, as the relative in-plane magnetization angle, ϕ, between the two ferromagnets varies. The ϕ-dependence of the self-consistent conductance curves in the trilayers can differ substantially from that obtained via a non-self-consistent approach. The zero bias forward conductance peak exhibits, as ϕ varies, resonance effects intricately associated with particular combinations of the geometrical and material parameters. We find, when the magnetizations are non-collinear, signatures of the anomalous Andreev reflections in the subgap regions of the angularly averaged conductances. When F_1 is half-metallic, the angularly averaged subgap conductance chiefly arises from anomalous Andreev reflection. The in-plane components of the spin current are strongly bias dependent, while the out-of-plane spin current component is only weakly dependent upon voltage. The components of the spin current aligned with the local exchange field of one of the F layers are conserved in that layer and in the S region, while they oscillate in the other layer. We compute the spin transfer torques, in connection with the oscillatory behavior of spin currents, and verify that the spin continuity equation is strictly obeyed in our method.

PACS numbers: 74.45.+c,74.78.Fk,75.75.-c

I. INTRODUCTION

Over the last two decades, significant progress in fabrication techniques has allowed the development of spintronics devices, such as spin valves,[1] that utilize both charge and spin degrees of freedom. Traditional spin valves consist of magnetic materials only. There is another important type of spintronics devices, involving ferromagnet (F)-superconductor (S) heterostructures. These heterostructures have also received much attention because of the fundamental physics related to the interplay between ferromagnetic and superconducting order. Their potential applications in spintronics include magnetic memory technology where information storage is accomplished via control of the magnetic moment bit. It is then crucial to have precise control over the magnetization direction. Spin transfer torque (STT) is one effect that affords such control. The generation of spin-polarized supercurrents may be used to obtain a superconducting STT acting on the magnetization of a ferromagnet. This effect may be utilized in high density nanotechnologies that require magnetic tunnel junctions. Thus, the dissipationless nature of the supercurrent flow offers a promising avenue in terms of low energy nanoscale manipulation of superconducting and magnetic orderings.

Although ferromagnetism and *s*-wave superconductivity seem incompatible because of the inherently opposite natures of their order parameter spin configurations, superconductivity can still be induced in the F layers of F-S layered structures by the superconducting proximity effects.[2] In essence, the superconducting proximity effects describe the leakage of superconductivity into a non-superconducting normal (N) or magnetic metal, as well as its depletion in S near the interface. However, proximity effects in F-S systems are very different from those in N-S structures due to the inherent exchange field in the F materials. As a consequence of this exchange field, the Cooper pair acquires a non-zero center-of-mass momentum[2–5] and the overall Cooper pair wavefunction oscillates spatially in the F regions. Owing to this oscillatory nature, many new physical phenomena emerge in F-S heterostructures such as oscillations of the superconducting transition temperature, T_c, with the thickness of the F layers.[2,3,6,7]

It is of fundamental importance that superconducting proximity effects are governed by Andreev reflection,[8] which is a process of electron-to-hole conversion at N-S or F-S interfaces, and it involves the creation or annihilation of a Cooper pair. Therefore, consideration of Andreev reflection is central when studying the transport properties of N-S[9,10] or F-S systems.[11–13] Of particular interest[9–13] is the behavior of the tunneling conductance in the subgap region, where hybrid systems can carry a supercurrent due to Andreev reflection. In conventional Andreev reflection, the reflected hole has opposite spin to the incident particle. Accordingly, the exchange field in the F materials that causes the splitting of spin bands has a significant effect on the tunneling conductance in the subgap region. Most important, the qualitative behavior of the conductance peak in the zero bias limit is strongly influenced by the degree of conduction electron spin polarization in the F materials.[11–14] Experimentally, this concept has been applied to quantify the spin polarization.[15–19]

An intriguing phenomenon in F-S structures is the induction of triplet pairing correlations.[20–24] These correlations are very important when studying transport phenomena such as those found in SFS Josephson junctions.[25–27] In contrast to

the short proximity length[5] of singlet Cooper pair condensates into F materials, the $m = \pm 1$ triplet pairing correlations are compatible with the exchange fields and hence largely immune to the pair breaking effect produced by the latter. However, for such correlations to be induced F-S structures must possess a spin-flip mechanism. Examples include a spin-dependent scattering potential at the F-S interface[28,29] and the introduction of another magnetic layer with a misoriented magnetic moment such as F_1SF_2 superconducting spin valves.[30] The pairing state of $m = \pm 1$ induced triplet correlations is at variance with the effects of *conventional* Andreev reflection, responsible for the generation of singlet Cooper pairs. Thus, recent studies[31–35] on the tunneling conductance propose the existence of *anomalous* Andreev reflection, that is, a reflected hole with the same spin as the incident particle can be Andreev reflected under the same circumstances as the generation of $m = \pm 1$ triplet pairing correlations becomes possible. In this view, triplet proximity effects are correlated with the process of this anomalous Andreev reflection. This will be confirmed and discussed in this work.

Another important geometry for a superconducting spin valve consists of a conventional spin valve with a superconductor layer on top: a F_1F_2S trilayer. By applying an external magnetic field, or switching via STT, one is able to control the relative orientation of the intrinsic magnetic moments and investigate the dependence[36–38] of physical properties such as T_c on the misorientation angle ϕ between the two magnetic layers. Due to the proximity effects, T_c is often found to be minimized when the magnetizations are approximately perpendicular to each other,[39] reflecting the presence of long range triplet correlations, induced in F_1F_2S trilayers. Their existence has been verified both theoretically[39] and experimentally.[36] The non-monotonic behavior of T_c as a function of ϕ has also been shown to be quantitatively[36] related to the long range triplet correlations, with excellent agreement between theory and experiment.

Motivated by these important findings, we will investigate here, in a fully self-consistent manner, the ϕ dependence of the tunneling conductance and other transport quantities of these F_1F_2S trilayers. Non-self-consistent theoretical studies of tunneling conductance have been performed on F_1F_2S trilayers in previous work.[34,40] However, as we shall see in Sec. II, only self-consistent methods guarantee that conservation laws are not violated and (see Sec. III) only then can one correctly predict the proximity effects on the angular dependence of transport properties. The spin-polarized tunneling conductance of F-S bilayers only, was studied in Refs. 12, 13, 41, and 42. Also, in traditional spin valves e.g. F_1-F_2 layered structures, the spin-polarized current generated in the F_1 layer can transfer angular momentum to the F_2 layer when their magnetic moments are not parallel to each other[1] via the effect of STT.[43,44] As a result, the spin current is not a conserved quantity and one needs a general law that relates local spin current to local STT.[31] The transport properties of F_1SF_2 structures, in particular the dependence on applied bias of the spin-transfer torque and the spin-polarized tunneling conductance have been previously studied.[31,45,46]

Here, we consider charge transport and both spin current and spin-transfer torque in F_1F_2S trilayers. In previous theoretical work, such as that mentioned above, when computing tunneling conductance of N-S and F-S structures, using methods based on the Blonder-Tinkham-Klapwijk (BTK) procedure[9,10,12,13,31,45,47] and quasi-classical approximations,[48] the superconducting pair amplitude was assumed to be a step function: a constant in S, dropping abruptly to zero at the N-S or F-S interface and then vanishing in the non-superconducting region. This assumption neglects proximity effects. Only qualitative predictions on the behavior of the tunneling conductance can be reliably made. Still, results exhibit many interesting features especially in F-S systems.[12,13] However, to fully account for the proximity effects, in the transport properties, one must use a self-consistent pair potential. This is because that reveals realistic information regarding the leakage and depletion of superconductivity. Also, as we shall discuss below, self-consistent solutions guarantee that conservation laws are satisfied. In Ref. 49, the tunneling conductance of F-S bilayers was extracted via self-consistent solutions of Bogoliubov-de Gennes (BdG) equations.[50] However, the numerical methods used there required awkward fitting procedures that led to appreciable uncertainties and precluded their application to trilayers. The findings indicated that the self-consistent tunneling conductances for the bilayer are quantitatively different from those computed in a non-self-consistent framework, thus demonstrating the importance of properly accounting for proximity effects in that situation. Here we report on a powerful **self-consistent** approach and use it to compute the tunneling conductance of F_1F_2S trilayers. It is based on the BTK method, incorporated into a transfer matrix procedure similar to that used[51] in Josephson junction calculations and simple F-S junctions within a Hubbard model[52]. As we shall demonstrate, this approach not only has the advantage of being more numerically efficient but also can be used to compute spin transport quantities. Thus, we are able to address many important points regarding both charge and spin transport in F_1F_2S trilayers, including the spin currents and spin-transfer torque, the proximity effects on the tunneling conductance, and the correlation between the anomalous Andreev reflection and the triplet correlations.

This paper is organized as follows: we present our self-consistent approach, and its application to compute the tunneling conductance, the spin-transfer torques, the spin current, and the proper way to ensure that conservation laws are satisfied, in Sec. II. In Sec. III we present the results. In Subsec. III A, we briefly compare the results of F-S bilayers obtained in our self-consistent approach with non-self-consistent ones. The rest of Subsec. III B includes our results for trilayers, that is, the main results of this work. The dependence on the tunneling conductance of F_1F_2S trilayers on the angle ϕ is extensively discussed as a function of geometrical and material parameters. Results for the effect of the anomalous Andreev reflection, the spin-transfer torque, and the spin current are also presented. We conclude with a recapitulation in Sec. IV.

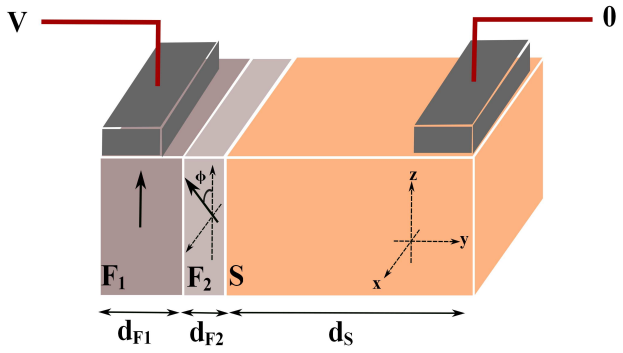

FIG. 1. (Color online) Schematic of the F_1F_2S trilayer. The exchange field, $\boldsymbol{h}$, denoted by a black solid arrow, is along the $+z$ direction in the outer magnetic layer (F_1) while within the inner magnetic layer (F_2), $\boldsymbol{h}$ is oriented at an angle ϕ in the $x-z$ plane. The outer magnetic layer and the superconducting layer are connected to electrodes that are biased with a finite voltage V.

II. METHODS

A. Description of the system

The geometry of our system is depicted in Fig. 1. We denote the outer ferromagnet as F_1 and the middle layer as F_2. We choose our coordinate system so that the interfaces are parallel to the $x-z$ plane, and infinite in extent, while the system has a finite width $d = d_{F_1} + d_{F_2} + d_S$ in the y direction.

The Hamiltonian appropriate to our system is,

$$\mathcal{H}_{eff} = \int d^3r \left\{ \sum_\alpha \psi^\dagger_\alpha(\mathbf{r}) \mathcal{H}_0 \psi_\alpha(\mathbf{r}) + \frac{1}{2}\left[\sum_{\alpha,\beta} \left(i\sigma_y\right)_{\alpha\beta} \Delta(\mathbf{r}) \psi^\dagger_\alpha(\mathbf{r}) \psi^\dagger_\beta(\mathbf{r}) + H.c. \right] - \sum_{\alpha,\beta} \psi^\dagger_\alpha(\mathbf{r}) (\mathbf{h}\cdot\boldsymbol{\sigma})_{\alpha\beta} \psi_\beta(\mathbf{r}) \right\}, \quad (1)$$

where $\mathcal{H}_0$ is the single-particle Hamiltonian, $\mathbf{h}$ is a Stoner exchange field that characterizes the magnetism, and $\boldsymbol{\sigma}$ are Pauli matrices. The superconducting pair potential $\Delta(\mathbf{r}) \equiv g(\mathbf{r})\langle\psi_\uparrow(\mathbf{r})\psi_\downarrow(\mathbf{r})\rangle$ is the product of pairing constant, $g(\mathbf{r})$, in the singlet channel, and the pair amplitude. We begin by writing down the BdG equations, which we will solve self-consistently for our F_1F_2S trilayers. By performing the generalized Bogoliubov transformation[50], $\psi_\sigma = \sum_n \left(u_{n\sigma}\gamma_n + \eta_\sigma v^*_{n\sigma}\gamma^\dagger_n\right)$, where $\sigma = (\uparrow,\downarrow)$ and $\eta_\sigma \equiv 1(-1)$ for spin-down (up), the Hamiltonian [Eq. (1)] can be diagonalized. We can then for our geometry rewrite[39] Eq. (1) as a quasi-one-dimensional eigensystem:

$$\begin{pmatrix} \mathcal{H}_0 - h_z & -h_x & 0 & \Delta \\ -h_x & \mathcal{H}_0 + h_z & \Delta & 0 \\ 0 & \Delta & -(\mathcal{H}_0 - h_z) & -h_x \\ \Delta & 0 & -h_x & -(\mathcal{H}_0 + h_z) \end{pmatrix} \begin{pmatrix} u_{n\uparrow} \\ u_{n\downarrow} \\ v_{n\uparrow} \\ v_{n\downarrow} \end{pmatrix} = \epsilon_n \begin{pmatrix} u_{n\uparrow} \\ u_{n\downarrow} \\ v_{n\uparrow} \\ v_{n\downarrow} \end{pmatrix}, \quad (2)$$

where the $u_{n\sigma}$ and $v_{n\sigma}$ are respectively the quasiparticle and quasihole amplitudes with spin σ. The exchange field vanishes in the S region, while in F_1 it is directed along z, $\mathbf{h} = h_1\hat{\mathbf{z}} \equiv \mathbf{h_1}$, and in F_2 it can rotate in the x–z plane, $\mathbf{h} = h_2(\sin\phi\hat{\mathbf{x}} + \cos\phi\hat{\mathbf{z}}) \equiv \mathbf{h_2}$. The single-particle Hamiltonian now reads[39] $\mathcal{H}_0 = -(1/2m)(d^2/dy^2) + \epsilon_\perp - E_F(y)$, where $\epsilon_\perp \equiv k^2_\perp/2m$ denotes the transverse kinetic energy in the $x-z$ plane. Also, $E_F(y) = E_{FS} \equiv k^2_{FS}/2m$ in the superconducting region and $E_F(y) = E_{FM} \equiv k^2_{FM}/2m$ in the ferromagnetic layers. Throughout this paper, we assume natural units $\hbar = k_B = 1$ and measure all energies in units of E_{FS}. To take into account the more realistic situation where the F materials can in general have different bandwidths than the S layer, we define (as in Ref. 49) a mismatch parameter Λ via $E_{FM} \equiv \Lambda E_{FS}$.

We are aiming here to solve the problem in a fully self consistent manner. The self-consistent pair potential $\Delta(y)$ can be expressed in terms of the quasi-particle and quasi-hole wavefunctions. Accordingly,

$$\Delta(y) = \frac{g(y)}{2} \sum_n{}' \left[u_{n\uparrow}(y)v^*_{n\downarrow}(y) + u_{n\downarrow}(y)v^*_{n\uparrow}(y)\right] \tanh\left(\frac{\epsilon_n}{2T}\right), \quad (3)$$

where the primed sum is over all eigenstates with energies ϵ_n smaller than a characteristic Debye energy, and $g(y)$ is the superconducting coupling constant in the S region and vanishes elsewhere. We obtain the self-consistent pair potential by solving Eqs. (2) and (3) following the iterative numerical procedures discussed in previous work.[24,39]

B. Application of the BTK method

The BTK formalism is a procedure to extract the transmitted and reflected amplitudes, and hence the conductance, from solutions to the BdG equations. This is accomplished by writing down the appropriate eigenfunctions in different regions. In this subsection, we review the relevant aspects of the formalism[9] for the non-self-consistent case (a step function pair potential) with the objective of establishing notation and methodology to describe, in the next subsection, the procedure to be used in the self-consistent case.

Consider first a spin-up quasi-particle with energy ϵ, incident into the left side labeled "F_1", in Fig. 1). Since the exchange fields in the F_1 and F_2 layers can be non-collinear, it follows from Eq. (2) that the spin-up (-down) quasi-particle wavefunction is not just coupled to the spin-down (-up) quasihole wavefunction, as is the case of F-S bilayers. Indeed,

the wavefunction in the F_1 layer is a linear combination of the original incident spin-up quasi-particle wavefunctions and various types of reflected wavefunctions, namely reflected spin-up and spin-down quasi-particle and quasi-hole wavefunctions (via both ordinary and Andreev reflections). We use a single column vector notation to represent these combinations,

$$\Psi_{F1,\uparrow} \equiv \begin{pmatrix} e^{ik^+_{\uparrow 1}y} + b_\uparrow e^{-ik^+_{\uparrow 1}y} \\ b_\downarrow e^{-ik^+_{\downarrow 1}y} \\ a_\uparrow e^{ik^-_{\uparrow 1}y} \\ a_\downarrow e^{ik^-_{\downarrow 1}y} \end{pmatrix} . \tag{4}$$

If the incident particle has spin down, the corresponding wavefunction in F_1 is

$$\Psi_{F1,\downarrow} \equiv \begin{pmatrix} b_\uparrow e^{-ik^+_{\uparrow 1}y} \\ e^{ik^+_{\downarrow 1}y} + b_\downarrow e^{-ik^+_{\downarrow 1}y} \\ a_\uparrow e^{ik^-_{\uparrow 1}y} \\ a_\downarrow e^{ik^-_{\downarrow 1}y} \end{pmatrix} . \tag{5}$$

In these expressions $k^\pm_{\sigma 1}$ are quasi-particle (+) and quasi-hole (−) wavevectors in the longitudinal direction y, and satisfy the relation,

$$k^\pm_{\sigma m} = \left[\Lambda(1 - \eta_\sigma h_m) \pm \epsilon - k_\perp^2\right]^{1/2}, \tag{6}$$

where $m = 1$ (as used above) or $m = 2$, used later. As mentioned above, all energies are in units of E_{FS} and, in addition, we measure all momenta in units of k_{FS}. In this simple case, one can easily distinguish the physical meaning of each individual wavefunction. For instance in Eq. (4), $a_\downarrow (0,0,0,1)^T e^{ik^-_{\downarrow 1}y}$ is the reflected spin-down quasi-hole wavefunction. The quasi-hole wavefunctions are the time reversed solutions of the BdG equations and carry a positive sign in the exponent for a left-going wavefunction. The relevant angles can be easily found in terms of wavevector components. Thus, e.g., the incident angle θ_i (for spin-up) at the $F_1 - F_2$ interface is $\theta_i = \tan^{-1}\left(k_\perp / k^+_{\uparrow 1}\right)$, and the Andreev reflected angle $\theta^-_{r\downarrow}$ for reflected spin-down quasi-hole wavefunction is $\theta^-_{r\downarrow} = \tan^{-1}\left(k_\perp / k^-_{\downarrow 1}\right)$. The conservation of transverse momentum leads to many important features[12,49] when one evaluates the angularly averaged tunneling conductance, as we will see below. For the intermediate layer F_2, the eigenfunction in general contains both left- and right-moving plane waves, that is,

$$\Psi_{F2} \equiv \begin{pmatrix} c_1 f^+_\uparrow e^{ik^+_{\uparrow 2}y} + c_2 f^+_\uparrow e^{-ik^+_{\uparrow 2}y} + c_3 g^+_\uparrow e^{ik^+_{\downarrow 2}y} + c_4 g^+_\uparrow e^{-ik^+_{\downarrow 2}y} \\ c_1 f^+_\downarrow e^{ik^+_{\uparrow 2}y} + c_2 f^+_\downarrow e^{-ik^+_{\uparrow 2}y} + c_3 g^+_\downarrow e^{ik^+_{\downarrow 2}y} + c_4 g^+_\downarrow e^{-ik^+_{\downarrow 2}y} \\ c_5 f^-_\uparrow e^{ik^-_{\uparrow 2}y} + c_6 f^-_\uparrow e^{-ik^-_{\uparrow 2}y} + c_7 g^-_\uparrow e^{ik^-_{\downarrow 2}y} + c_8 g^-_\uparrow e^{-ik^-_{\downarrow 2}y} \\ c_5 f^-_\downarrow e^{ik^-_{\uparrow 2}y} + c_6 f^-_\downarrow e^{-ik^-_{\uparrow 2}y} + c_7 g^-_\downarrow e^{ik^-_{\downarrow 2}y} + c_8 g^-_\downarrow e^{-ik^-_{\downarrow 2}y} \end{pmatrix}, \tag{7}$$

where $k^\pm_{\uparrow 2}$ and $k^\pm_{\downarrow 2}$ are defined in Eq. (6). The ± indices are defined as previously, and the up and down arrows refer to F_1. The eigenspinors f and g that correspond to spin parallel or antiparallel to $\mathbf{h_2}$ respectively, are given, for $0 \le \phi \le \pi/2$, by the expression,

$$\begin{pmatrix} f^+_\uparrow \\ f^+_\downarrow \end{pmatrix} = \frac{1}{\mathcal{N}} \begin{pmatrix} 1 \\ \frac{1-\cos\phi}{\sin\phi} \end{pmatrix} = \begin{pmatrix} f^-_\uparrow \\ -f^-_\downarrow \end{pmatrix}; \quad \begin{pmatrix} g^+_\uparrow \\ g^+_\downarrow \end{pmatrix} = \frac{1}{\mathcal{N}} \begin{pmatrix} -\frac{\sin\phi}{1+\cos\phi} \\ 1 \end{pmatrix} = \begin{pmatrix} -g^-_\uparrow \\ g^-_\downarrow \end{pmatrix} \tag{8}$$

with the normalization constant $\mathcal{N} = \sqrt{2/1+\cos\phi}$. These spinors reduce to those for pure spin-up and spin-down quasi-particles and holes when $\phi = 0$, corresponding to a uniform magnetization along z. One can also easily see that the particular wavefunction of Eq. (7), $c_1 \left(f^+_\uparrow, f^+_\downarrow, 0, 0\right)^T e^{ik^+_{\uparrow 2}y}$ denotes a quasi-particle with spin parallel to the exchange field in F_2. When $\pi/2 < \phi \le \pi$, these eigenspinors read

$$\begin{pmatrix} f^+_\uparrow \\ f^+_\downarrow \end{pmatrix} = \frac{1}{\mathcal{N}} \begin{pmatrix} \frac{\sin\phi}{1-\cos\phi} \\ 1 \end{pmatrix} = \begin{pmatrix} -f^-_\uparrow \\ f^-_\downarrow \end{pmatrix}; \quad \begin{pmatrix} g^+_\uparrow \\ g^+_\downarrow \end{pmatrix} = \frac{1}{\mathcal{N}} \begin{pmatrix} 1 \\ -\frac{1+\cos\phi}{\sin\phi} \end{pmatrix} = \begin{pmatrix} g^-_\uparrow \\ -g^-_\downarrow \end{pmatrix} \tag{9}$$

with $\mathcal{N} = \sqrt{2/1-\cos\phi}$.

In this subsection where we are still assuming a non-self-consistent stepwise potential equal to Δ_0 throughout the S region and to zero elsewhere, we have the superconducting coherence factors, $\sqrt{2}u_0 = \left[\left(\epsilon + \sqrt{\epsilon^2 - \Delta_0^2}\right)/\epsilon\right]^{1/2}$ and $\sqrt{2}v_0 = \left[\left(\epsilon - \sqrt{\epsilon^2 - \Delta_0^2}\right)/\epsilon\right]^{1/2}$. In this case the right-going eigenfunctions on the S side can be written as,

$$\Psi_S \equiv \begin{pmatrix} t_1 u_0 e^{ik^+ y} + t_4 v_0 e^{-ik^- y} \\ t_2 u_0 e^{ik^+ y} + t_3 v_0 e^{-ik^- y} \\ t_2 v_0 e^{ik^+ y} + t_3 u_0 e^{-ik^- y} \\ t_1 v_0 e^{ik^+ y} + t_4 u_0 e^{-ik^- y} \end{pmatrix}, \tag{10}$$

where, $k^\pm = \left[1 \pm \sqrt{\epsilon^2 - \Delta_0^2} - k_\perp^2\right]^{1/2}$ are quasi-particle (+) and quasi-hole (-) wavevectors in the S region. By using continuity of the four-component wavefunctions and their first derivatives at both interfaces, one can obtain all sixteen unknown coefficients in the above expressions for the wavefunctions by solving a set of linear equations of the form $\mathcal{M}_{F1} x_{F1,\sigma} = \mathcal{M}_{F2} x_{F2}$ at the $F_1 - F_2$ interface and $\tilde{\mathcal{M}}_{F2} x_{F2} = \mathcal{M}_S x_S$ at the $F_2 - S$ interface simultaneously, where

$$x^T_{F1,\uparrow} = (1, b_\uparrow, 0, b_\downarrow, 0, a_\uparrow, 0, a_\downarrow) \tag{11a}$$

$$x^T_{F1,\downarrow} = (0, b_\uparrow, 1, b_\downarrow, 0, a_\uparrow, 0, a_\downarrow) \tag{11b}$$

$$x^T_{F2} = (c_1, c_2, c_3, c_4, c_5, c_6, c_7, c_8) \tag{11c}$$

$$x^T_S = (t_1, 0, t_2, 0, t_3, 0, t_4, 0), \tag{11d}$$

and $\mathcal{M}_{F1}$, $\mathcal{M}_{F2}$, $\tilde{\mathcal{M}}_{F2}$, and $\mathcal{M}_S$ are appropriate 8×8 matrices, which are straightforward to write down. Use of these coefficients gives us all the reflected and transmitted amplitudes a_σ and b_σ which are used to compute the conductance, as discussed in the next two subsections.

C. Transfer matrix self consistent method

The non-self-consistent step potential assumption is largely unrealistic. Proximity effects lead to a complicated oscillatory

behavior of the superconducting order parameter in the F layers and to the generation[2,21–25,30,32] of triplet pairs as discussed in Sec. I. The concomitant depletion of the pair amplitudes near the F-S interface means that unless the superconductor is thick enough, the pair amplitude does not saturate to its bulk value even deep inside the S regions. Furthermore, as we shall emphasize below, lack of self consistency may lead to violation of charge conservation: hence, while non-self-consistent approximations might be sometimes adequate for equilibrium calculations, their use must be eschewed for transport. Therefore, one should generally use a self-consistent pair potential that is allowed to spatially vary, as required by Eq. (3), and hence results in a minimum in the free energy of the system.

We begin by extending the BTK formalism to the spatially varying self-consistent pair potential obtained as explained below Eq. (3). Although the self-consistent solutions of the BdG equations reveal that the pair amplitudes are non-zero in the non-superconducting regions due to the proximity effects, the pair potential vanishes in these regions since $g(y) \equiv 0$ there. Therefore, one can still use Eqs. (4) and (5), with (7), for the wavefunctions in the F_1 and F_2 regions. To deal with the spatially varying pair potential on the S side, we divide it into many very thin layers with microscopic thicknesses of order k_{FS}^{-1}. We treat each layer as a very thin superconductor with a constant pair potential, Δ_i, as obtained from the self-consistent procedure. We are then able to write the eigenfunctions of each superconducting layer corresponding to that value of the pair potential. For example, in the i-th layer, the eigenfunction should contain all left and right going solutions, and it reads:

$$\Psi_{Si} \equiv \begin{pmatrix} t_{1i}u_i e^{ik_i^+ y} + \bar{t}_{1i}u_i e^{-ik_i^+ y} + t_{4i}v_i e^{-ik_i^- y} + \bar{t}_{4i}v_i e^{ik_i^- y} \\ t_{2i}u_i e^{ik_i^+ y} + \bar{t}_{2i}u_i e^{-ik_i^+ y} + t_{3i}v_i e^{-ik_i^- y} + \bar{t}_{3i}v_i e^{ik_i^- y} \\ t_{2i}v_i e^{ik_i^+ y} + \bar{t}_{2i}v_i e^{-ik_i^+ y} + t_{3i}u_i e^{-ik_i^- y} + \bar{t}_{3i}u_i e^{ik_i^- y} \\ t_{1i}v_i e^{ik_i^+ y} + \bar{t}_{1i}v_i e^{-ik_i^+ y} + t_{4i}u_i e^{-ik_i^- y} + \bar{t}_{4i}v_i e^{ik_i^- y} \end{pmatrix}, \quad (12)$$

where, $k_i^{\pm} = \left[1 \pm \sqrt{\epsilon^2 - \Delta_i^2} - k_\perp^2\right]^{1/2}$, and Δ_i represents the strength of the normalized self consistent pair potential in the i-th superconducting layer. The superconducting coherence factors u_i and v_i depend on Δ_i in the standard way. All the coefficients in Eq. (12) are unknown, and remain to be determined. However, in the outermost S layer (rightmost in our convention) the eigenfunctions are of a form identical to Eq. (10) but with different locally constant pair potential.

We see then that the price one has to pay for including the proximity effects is the need to compute a very large number of coefficients. To do so, we adopt here a transfer matrix method to solve for these unknowns.[51] If one considers the interface between the i-th and the $(i+1)$-th layer, we have the linear relation $\tilde{\mathcal{M}}_i x_i = \mathcal{M}_{i+1} x_{i+1}$, where, for a generic i,

$$x_i^T = (t_{1i}, \bar{t}_{1i}, t_{2i}, \bar{t}_{2i}, t_{3i}, \bar{t}_{3i}, t_{4i}, \bar{t}_{4i}), \quad (13)$$

and the matrices, $\tilde{\mathcal{M}}_i$ and $\mathcal{M}_{i+1}$, can be written as discussed in connection with Eq. (11). The coefficients in the $(i+1)$-th layer can be obtained in terms of those in the i-th layer as $x_{i+1} = \mathcal{M}_{i+1}^{-1}\tilde{\mathcal{M}}_i x_i$. In the same way, for the interface between the $(i-1)$-th layer and the i-th layer, we can write $x_i = \mathcal{M}_i^{-1}\tilde{\mathcal{M}}_{i-1}x_{i-1}$. From the above relations, one can write down the relation between x_{i+1} and x_{i-1}, i.e. $x_{i+1} = \mathcal{M}_{i+1}^{-1}\tilde{\mathcal{M}}_i\mathcal{M}_i^{-1}\tilde{\mathcal{M}}_{i-1}x_{i-1}$. By iteration of this procedure, one can "transfer" the coefficients layer by layer and eventually relate the coefficients of the rightmost layer, x_n, to those of the leftmost layer in S and then on to the inner ferromagnetic layer F_2:

$$x_n = \mathcal{M}_n^{-1}\tilde{\mathcal{M}}_{n-1}\mathcal{M}_{n-1}^{-1}\cdots\tilde{\mathcal{M}}_1\mathcal{M}_1^{-1}\tilde{\mathcal{M}}_{F2}x_{F2} \quad (14)$$

By solving Eq. (14) together with $\mathcal{M}_{F1}x_{F1} = \mathcal{M}_{F2}x_{F2}$, we obtain all the coefficients in the F_1 region, where the wavefunction is *formally* still described by the expressions given in Eqs. (4) and (5). Of course, all coefficients involved, including the energy dependent a_σ and b_σ values from which (see below) the conductance is extracted, are quite different from those in a non-self-consistent calculation. These differences will be reflected in our results. One can also prove that, when the pair potential in S is a constant (non-self-consistent), then $\mathcal{M}_{i+1} = \tilde{\mathcal{M}}_i$ and therefore Eq. (14) becomes $x_n = x_1 = \mathcal{M}_1^{-1}\tilde{\mathcal{M}}_{F2}x_{F2}$. This is formally identical to that we have seen in our discussion of the non-self-consistent formalism.

This efficient technique, besides allowing us to determine all the reflected and transmitted amplitudes in the outermost layers, permits us to perform a consistency check by recomputing the self-consistent solutions to the BdG equations (the eigenfunctions). Once we have determined the amplitudes x_{F1}, x_{F2}, and x_n, we can use them to find the amplitudes in any intermediate layer by "transferring" back the solutions. For example, the coefficients x_{n-1} can be found by using $x_n = \mathcal{M}_n^{-1}\tilde{\mathcal{M}}_{n-1}x_{n-1}$ if we know the coefficient x_n for the rightmost layer. Knowledge of these coefficients in every region yields again the self-consistent wavefunctions of the system. These of course should be the same as the eigenfunctions found in the original procedure. Although the numerical computations involved in this consistency check are rather intensive, it is worthwhile to perform them: we have verified that, by plugging these solutions into Eq. (3) and considering all possible solutions with all possible incident angles to the BdG equations, the output pair potential obtained from the transport calculation is the same as the input pair potential obtained by direct diagonalization. This would obviously not have been the case if the initial pair potential had not been fully self consistent to begin with. The reflected and transmitted amplitudes calculated from the self-consistent solutions are in general very different from the non-self-consistent ones and lead to different quantitative behavior of the tunneling conductance, as we shall discuss in section III.

D. Charge conservation

We discuss now the important issue of the charge conservation laws. In transport calculations, it is fundamental to assure that they are not violated[53]. From the Heisenberg equation

$$\frac{\partial}{\partial t}\langle\rho(\mathbf{r})\rangle = i\left\langle\left[\mathcal{H}_{eff}, \rho(\mathbf{r})\right]\right\rangle. \quad (15)$$

By computing the above commutator, we arrive at the following continuity condition

$$\frac{\partial}{\partial t}\langle\rho(\mathbf{r})\rangle + \nabla\cdot\mathbf{j} = -4e\mathrm{Im}\left[\Delta(\mathbf{r})\left\langle\psi_\uparrow^\dagger(\mathbf{r})\psi_\downarrow^\dagger(\mathbf{r})\right\rangle\right]. \tag{16}$$

In the steady state, which is all that we are considering here, the first term on the left is omitted. Eqn. (16) is then simply an expression for the divergence of the current. In our quasi one-dimensional system, and in terms of our wavefunctions, the conservation law can be rewritten as:

$$\frac{\partial j_y(y)}{\partial y} = 2e\mathrm{Im}\left\{\Delta(y)\sum_n\left[u_{n\uparrow}^* v_{n\downarrow} + u_{n\downarrow}^* v_{n\uparrow}\right]\tanh\left(\frac{\epsilon_n}{2T}\right)\right\} \tag{17}$$

When the system is in equilibrium the self-consistency condition on the pair potential causes the right hand side of Eqs. (16) or (17) to vanish. This would **not** necessarily be the case if a non-self-consistent[54] solution were used.[55] It was shown that charge conservation is only guaranteed when self consistency is adhered to in microscopic Josephson junctions.[56] Current-voltage calculations for N-S heterostructures show that self-consistency is crucial to properly account for all of the Andreev scattering channels arising when the current is constant throughout the system.[57] While non-self-consistent solutions are less computationally demanding, their validity when calculating transport quantities in the nonequilibrium regime is always suspect.

In the problem we are considering, there exists a finite voltage bias V between the two leads of the system (see Fig. 1). This finite bias leads to a non-equilibrium quasi-particle distribution and results of course in a net current. Still, charge conservation must hold. To see how this works in this non-equilibrium case we first write down the net quasi-particle charge density in the $T\to 0$ limit (the case we consider here) by considering the excited state $|\mathbf{k_1}\mathbf{k_2}\cdots\rangle$ caused by the finite bias V. Thus, this excited state contains all single particle states $|\mathbf{k_j}\rangle$ ($j = 1, 2, \cdots$) with energies less than eV. For simplicity, let us first consider the contribution by a single-particle state. We use $|\mathbf{k}\rangle$ to characterize this single particle state with an incident wavevector $\mathbf{k} = \mathbf{k}_\perp + k\hat{\mathbf{y}}$ and energy $\epsilon_\mathbf{k}$. The charge density associated with it is written as

$$\begin{aligned}
\rho &= -e\sum_\sigma\left\langle\mathbf{k}\left|\psi_\sigma^\dagger\psi_\sigma\right|\mathbf{k}\right\rangle \qquad (18)\\
&= -e\sum_{n\sigma}\left(|u_{n\sigma}|^2\left\langle\mathbf{k}\left|\gamma_n^\dagger\gamma_n\right|\mathbf{k}\right\rangle + |v_{n\sigma}|^2\left\langle\mathbf{k}\left|\gamma_n\gamma_n^\dagger\right|\mathbf{k}\right\rangle\right)\\
&= -e\sum_{n\sigma}\left(|u_{n\sigma}|^2\left\langle\mathbf{k}\left|\gamma_n^\dagger\gamma_n\right|\mathbf{k}\right\rangle + |v_{n\sigma}|^2\left\langle\mathbf{k}\left|1-\gamma_n^\dagger\gamma_n\right|\mathbf{k}\right\rangle\right)\\
&= -e\sum_{n\sigma}|v_{n\sigma}|^2 - e\sum_{n\sigma}\left(|u_{n\sigma}|^2 - |v_{n\sigma}|^2\right)\delta_{n\mathbf{k}}\\
&= -e\sum_{n\sigma}|v_{n\sigma}|^2 - e\sum_\sigma\left(|u_{\mathbf{k}\sigma}|^2 - |v_{\mathbf{k}\sigma}|^2\right)
\end{aligned}$$

The first term represents the ground state charge density. For a generic excited state, $|\mathbf{k_1}\mathbf{k_2}\cdots\rangle$, that can contain many single-particle states, one need to sum over all single-particle states for the charge density such that

$$\rho = -e\sum_{n\sigma}|v_{n\sigma}|^2 - e\sum_{\epsilon_\mathbf{k}<eV}\sum_\sigma\left(|u_{\mathbf{k}\sigma}|^2 - |v_{\mathbf{k}\sigma}|^2\right). \tag{19}$$

The quasi-particle current density from this generic excited state can also be computed,

$$\begin{aligned}
j_y &= -\frac{e}{2m}\sum_{\epsilon_\mathbf{k}<eV}\sum_\sigma\left\langle -i\psi_\sigma^\dagger\frac{\partial}{\partial y}\psi_\sigma + i\left(\frac{\partial}{\partial y}\psi_\sigma^\dagger\right)\psi_\sigma\right\rangle_\mathbf{k} \qquad (20)\\
&= -\frac{e}{m}\mathrm{Im}\left[\sum_{n\sigma}v_{n\sigma}\frac{\partial v_{n\sigma}^*}{\partial y} + \sum_{\epsilon_\mathbf{k}<eV}\sum_\sigma\left(u_{\mathbf{k}\sigma}^*\frac{\partial u_{\mathbf{k}\sigma}}{\partial y} + v_{\mathbf{k}\sigma}^*\frac{\partial v_{\mathbf{k}\sigma}}{\partial y}\right)\right]\\
&= -\frac{e}{m}\mathrm{Im}\left[\sum_{\epsilon_\mathbf{k}<eV}\sum_\sigma\left(u_{\mathbf{k}\sigma}^*\frac{\partial u_{\mathbf{k}\sigma}}{\partial y} + v_{\mathbf{k}\sigma}^*\frac{\partial v_{\mathbf{k}\sigma}}{\partial y}\right)\right],
\end{aligned}$$

where $\langle\ldots\rangle_\mathbf{k}$ is a shorthand notation of $\langle\mathbf{k}|\ldots|\mathbf{k}\rangle$. The first term in the second line vanishes because it represents the net current for the system in the ground state with a real pair potential. The right hand side of the continuity equation, Eq. (17), becomes $-4e\mathrm{Im}\left[\Delta\sum_{\epsilon_\mathbf{k}<eV}\left(u_{\mathbf{k}\uparrow}^* v_{\mathbf{k}\downarrow} + v_{\mathbf{k}\uparrow}u_{\mathbf{k}\downarrow}^*\right)\right]$ and is responsible for the interchange between the quasi-particle current density and the supercurrent density[9]. We have numerically verified that by properly including these terms, all of our numerical results for the current density are constant throughout the whole system.

E. Extraction of the conductance

We are now in a position to compute the differential tunneling conductances. We begin by discussing the extraction of the conductance from the BTK theory. As we mentioned in the previous subsection, the finite bias V and the resulting non-equilibrium distribution leads to an electric current flowing in the junction. In the BTK theory, this current can be evaluated from the following[9] expression,

$$I(V) = \int G(\epsilon)\left[f(\epsilon - eV) - f(\epsilon)\right]d\epsilon, \tag{21}$$

where f is the Fermi function. The energy dependent tunneling conductance, $G(\epsilon) = \partial I/\partial V|_{V=\epsilon}$ in the low-T limit, is given as:

$$\begin{aligned}
G(\epsilon,\theta_i) &= \sum_\sigma P_\sigma G_\sigma(\epsilon,\theta_i) \qquad (22)\\
&= \sum_\sigma P_\sigma\left(1 + \frac{k_{\uparrow 1}^-}{k_{\sigma 1}^+}|a_\uparrow|^2 + \frac{k_{\downarrow 1}^-}{k_{\sigma 1}^+}|a_\downarrow|^2 - \frac{k_{\uparrow 1}^+}{k_{\sigma 1}^+}|b_\uparrow|^2 - \frac{k_{\downarrow 1}^+}{k_{\sigma 1}^+}|b_\downarrow|^2\right),
\end{aligned}$$

where we have used, as is customary, natural units of conductance (e^2/h). In the above expression the different k components are as explained in subsection II B (see e.g. Eq. (6)) and the a_σ and b_σ are as defined in Eqns. (4) and (5). These coefficients, which are of course energy dependent, are calculated using the self-consistent transfer matrix technique of subsection II C. Therefore, even though Eq. (22) is formally the same in the self-consistent and non-self-consistent cases, the results for the reflection amplitudes or probabilities involved, $|a_\uparrow|^2$, $|a_\downarrow|^2$, $|b_\uparrow|^2$, and $|b_\downarrow|^2$ are different in these two schemes. The angle θ_i is the incident angle, discussed in terms of $\mathbf{k}$ components below Eq. (6). The weight factor $P_\sigma \equiv (1 - h_1\eta_\sigma)/2$

accounts for the number of available states for spin-up and spin-down bands in the outer electrode. The tunneling conductance can also be interpreted as the transmission coefficient for electrical current. The method enables us also to compute the current density directly from the wavefunctions, Eqs. (4) and (5), in the F_1 layer by using Eq. (20) and we have been able to verify that the resulting current density is identical to the terms inside the bracket in the expression of $G(\epsilon)$, Eq. (22). In other words, in the low-T limit the continuum-limit version of Eq. (20) is equivalent to Eq. (21).

The conductance results Eq. (22) also depend on the incident angle of electrons, θ_i. Experimentally, one can measure the forward conductance, $\theta_i = 0$, via point contacts or, in most other experimental conditions, an angular average. Consequently, it is worthwhile to compute the angularly averaged conductance by using the following definitions,

$$\langle G_\sigma(\epsilon)\rangle = \frac{\int_0^{\theta_{c\sigma}} d\theta_i \cos\theta_i G_\sigma(\epsilon,\theta_i)}{\int_0^{\theta_{c\sigma}} d\theta_i \cos\theta_i}, \tag{23}$$

and

$$\langle G\rangle = \sum_\sigma P_\sigma \langle G_\sigma\rangle, \tag{24}$$

where the critical angle $\theta_{c\sigma}$ is in general different for spin-up and spin-down bands. This critical angle arises from the conservation of transverse momentum and the corresponding Snell law:

$$\begin{aligned}&\sqrt{\left({k^+_{\sigma 1}}^2 + k_\perp^2\right)}\sin\theta_i = \sqrt{\left({k^+_{\sigma' 1}}^2 + k_\perp^2\right)}\sin\theta^+_{r\sigma'} \\ &= \sqrt{\left({k^-_{\sigma' 1}}^2 + k_\perp^2\right)}\sin\theta^-_{r\sigma'} = \sin\theta_S,\end{aligned} \tag{25}$$

where we continue to measure wavevectors in units of k_{FS}. The angles $\theta^\pm_{r\sigma}$ satisfy $\tan^{-1}\left(k_\perp/k^\pm_{\sigma 1}\right)$, and the σ and σ' are each $\uparrow$ or $\downarrow$. The last equality in Eq. (25) represents the case of the transmitted wave in S, and θ_S is the transmitted angle. Although the self-consistent pair potential varies in S and so do the quasi-particle (hole) wavevectors, we here need only consider the transmitted angle θ_S in the rightmost layer: this follows in the same way as the usual Snell's law in a layered system, as given in elementary textbooks. From Eq. (25), one can determine the critical angles for different channels. Consider, e.g., a spin-up electron incident from F_1 without any Fermi wavevector mismatch, i.e. $\Lambda = 1$. Since we are only concerned with the case that the bias of tunneling junctions is of the order of superconducting gap and therefore much smaller than the Fermi energy, the approximate magnitude of the incident wavevector is $\sqrt{1+h_1}$, the Andreev approximation. We substitute this and similar expressions into Eq. (25) and, with the help of Eq. (6), we obtain

$$\sqrt{1+h_1}\sin\theta_i = \sqrt{1-h_1}\sin\theta^-_{r\downarrow} = \sin\theta_S. \tag{26}$$

One can straightforwardly verify that, when the relation $\theta_i > \sin^{-1}[((1-h_1)/(1+h_1))^{1/2}]$ is satisfied for the incident angle, the conventional Andreev reflection becomes an evanescent wave[13]. In this case, the conventional Andreev reflection does not contribute to the angular averaging. On the other hand, if the energy ϵ of the incident electron is less than the saturated value of the superconducting pair amplitude in S, all the contribution to the conductance from the transmitted waves in S also vanishes because $k^\pm$ acquires an imaginary part. However, even the condition that ϵ is greater than the saturated superconducting amplitude does not guarantee that the contribution from the transmitted waves to the conductance is non-vanishing. One still needs to consider the transmitted critical angle $\sin^{-1}[1/(1+h_1)^{1/2}]$. We define the critical angle $\theta_{c\sigma}$ to be the largest one among all the reflected and transmitted critical angles. It is obvious that the critical angles $\theta_{c\sigma}$ are different for spin-up and spin-down bands when $h_1 \neq 0$.

F. Spin transport

We consider now the spin-transfer torque and the spin current. As the charge carriers that flow through our system, along the y direction in our convention, are spin polarized, the STT provides an additional probe of the spin degree of freedom. Unlike the charge current, that must be a constant throughout the system, the spin current density is generally not a conserved quantity in the ferromagnet regions as we will demonstrate below. The discussion in Sec. II D on how the BTK formalism deals with the charge current can be extended to compute these spin dependent transport quantities. We need here the continuity equation for the local magnetization $\mathbf{m} \equiv -\mu_B \sum_\sigma \left\langle \psi^\dagger_\sigma \boldsymbol{\sigma} \psi_\sigma \right\rangle$, where μ_B is the Bohr magneton. By using the Heisenberg equation $\frac{\partial}{\partial t}\langle \mathbf{m}(\mathbf{r})\rangle = i\left\langle \left[\mathcal{H}_{eff}, \mathbf{m}(\mathbf{r})\right]\right\rangle$ we obtain the relation:

$$\frac{\partial}{\partial t}\langle m_i\rangle + \frac{\partial}{\partial y} S_i = \tau_i, \quad i = x,y,z \tag{27}$$

where $\boldsymbol{\tau}$ is the spin-transfer torque, $\boldsymbol{\tau} \equiv 2\mathbf{m}\times\mathbf{h}$, and the spin current density S_i is given by

$$S_i \equiv \frac{i\mu_B}{2m}\sum_\sigma \left\langle \psi^\dagger_\sigma \sigma_i \frac{\partial \psi_\sigma}{\partial y} - \frac{\partial \psi^\dagger_\sigma}{\partial y}\sigma_i \psi_\sigma \right\rangle. \tag{28}$$

The spin current density reduces from a tensor form to a vector because of the quasi-one-dimensional nature of our geometry. From Eq. (27), we can see that $\mathbf{S}$ is a local physical quantity and $\boldsymbol{\tau}$ is responsible for the change of local magnetizations due to the flow of spin-polarized currents. As we shall see in Sec. III, the conservation law (with the source torque term) for the spin density is fundamental and one has to check it is not violated when studying these transport quantities.

In the low-T limit and with the presence of a finite bias, the non-equilibrium local magnetizations $m_i \equiv$

$\sum_{\epsilon_{\mathbf{k}}<eV}\sum_\sigma -\mu_B\langle\psi^\dagger_\sigma\sigma_i\psi_\sigma\rangle_{\mathbf{k}}$ in Eq. (27) reads

$$m_x = -\mu_B\Bigg[\sum_n\left(-v_{n\uparrow}v^*_{n\downarrow}-v_{n\downarrow}v^*_{n\uparrow}\right) + \sum_{\epsilon_{\mathbf{k}}<eV}\left(u^*_{\mathbf{k}\uparrow}u_{\mathbf{k}\downarrow}+v_{\mathbf{k}\uparrow}v^*_{\mathbf{k}\downarrow}+u^*_{\mathbf{k}\downarrow}u_{\mathbf{k}\uparrow}+v_{\mathbf{k}\downarrow}v^*_{\mathbf{k}\uparrow}\right)\Bigg] \tag{29a}$$

$$m_y = -\mu_B\Bigg[i\sum_n\left(v_{n\uparrow}v^*_{n\downarrow}-v_{n\downarrow}v^*_{n\uparrow}\right) -i\sum_{\epsilon_{\mathbf{k}}<eV}\left(u^*_{\mathbf{k}\uparrow}u_{\mathbf{k}\downarrow}+v_{\mathbf{k}\uparrow}v^*_{\mathbf{k}\downarrow}-u^*_{\mathbf{k}\downarrow}u_{\mathbf{k}\uparrow}-v_{\mathbf{k}\downarrow}v^*_{\mathbf{k}\uparrow}\right)\Bigg] \tag{29b}$$

$$m_z = -\mu_B\Bigg[\sum_n\left(|v_{n\uparrow}|^2-|v_{n\downarrow}|^2\right) + \sum_{\epsilon_{\mathbf{k}}<eV}\left(|u_{\mathbf{k}\uparrow}|^2-|v_{\mathbf{k}\uparrow}|^2-|u_{\mathbf{k}\downarrow}|^2+|v_{\mathbf{k}\downarrow}|^2\right)\Bigg], \tag{29c}$$

where the first summations in the expressions for m_i denote the ground state local magnetizations. The second summations appear as a consequence of the finite bias between electrodes. The expressions for the corresponding spin currents,

$$S_i \equiv \frac{i\mu_B}{2m}\sum_{\epsilon_{\mathbf{k}}<eV}\sum_\sigma\left\langle\psi^\dagger_\sigma\sigma_i\frac{\partial\psi_\sigma}{\partial y}-\frac{\partial\psi^\dagger_\sigma}{\partial y}\sigma_i\psi_\sigma\right\rangle_{\mathbf{k}}, \tag{30}$$

becomes

$$S_x = \frac{-\mu_B}{m}\mathrm{Im}\Bigg[\sum_n\left(-v_{n\uparrow}\frac{\partial v^*_{n\downarrow}}{\partial y}-v_{n\downarrow}\frac{\partial v^*_{n\uparrow}}{\partial y}\right) + \sum_{\epsilon_{\mathbf{k}}<eV}\left(u^*_{\mathbf{k}\uparrow}\frac{\partial u_{\mathbf{k}\downarrow}}{\partial y}+v_{\mathbf{k}\uparrow}\frac{\partial v^*_{\mathbf{k}\downarrow}}{\partial y}+u^*_{\mathbf{k}\downarrow}\frac{\partial u_{\mathbf{k}\uparrow}}{\partial y}+v_{\mathbf{k}\downarrow}\frac{\partial v^*_{\mathbf{k}\uparrow}}{\partial y}\right)\Bigg] \tag{31a}$$

$$S_y = \frac{\mu_B}{m}\mathrm{Re}\Bigg[\sum_n\left(-v_{n\uparrow}\frac{\partial v^*_{n\downarrow}}{\partial y}+v_{n\downarrow}\frac{\partial v^*_{n\uparrow}}{\partial y}\right) + \sum_{\epsilon_{\mathbf{k}}<eV}\left(u^*_{\mathbf{k}\uparrow}\frac{\partial u_{\mathbf{k}\downarrow}}{\partial y}+v_{\mathbf{k}\uparrow}\frac{\partial v^*_{\mathbf{k}\downarrow}}{\partial y}-u^*_{\mathbf{k}\downarrow}\frac{\partial u_{\mathbf{k}\uparrow}}{\partial y}-v_{\mathbf{k}\downarrow}\frac{\partial v^*_{\mathbf{k}\uparrow}}{\partial y}\right)\Bigg] \tag{31b}$$

$$S_z = \frac{-\mu_B}{m}\mathrm{Im}\Bigg[\sum_n\left(v_{n\uparrow}\frac{\partial v^*_{n\uparrow}}{\partial y}-v_{n\downarrow}\frac{\partial v^*_{n\downarrow}}{\partial y}\right) + \sum_{\epsilon_{\mathbf{k}}<eV}\left(u^*_{\mathbf{k}\uparrow}\frac{\partial u_{\mathbf{k}\uparrow}}{\partial y}-v_{\mathbf{k}\uparrow}\frac{\partial v^*_{\mathbf{k}\uparrow}}{\partial y}-u^*_{\mathbf{k}\downarrow}\frac{\partial u_{\mathbf{k}\downarrow}}{\partial y}+v_{\mathbf{k}\downarrow}\frac{\partial v^*_{\mathbf{k}\downarrow}}{\partial y}\right)\Bigg]. \tag{31c}$$

The first summations in Eq. (31) represent the static spin current densities when there is no bias. The static spin current does not need to vanish, since a static spin-transfer torque may exist near the boundary of two magnets with misaligned exchange fields. The finite bias leads to a non-equilibrium quasi-particle distribution for the system and results in non-static spin current densities that are represented by the second summation in Eq. 31. Obviously, the spin-transfer torque has to vanish in the superconductor where the exchange field is zero. It is conventional to normalize $\mathbf{m}$ to[30] $-\mu_B(N_\uparrow+N_\downarrow)$, where the number densities $N_\uparrow = k_{FS}^3(1+h_m)^{3/2}/(6\pi^2)$ and $N_\downarrow = k_{FS}^3(1-h_m)^{3/2}/(6\pi^2)$. Following this convention, we normalize $\boldsymbol{\tau}$ to $-\mu_B(N_\uparrow+N_\downarrow)E_{FS}$ and $\mathbf{S}$ to $-\mu_B(N_\uparrow+N_\downarrow)E_{FS}/k_{FS}$.

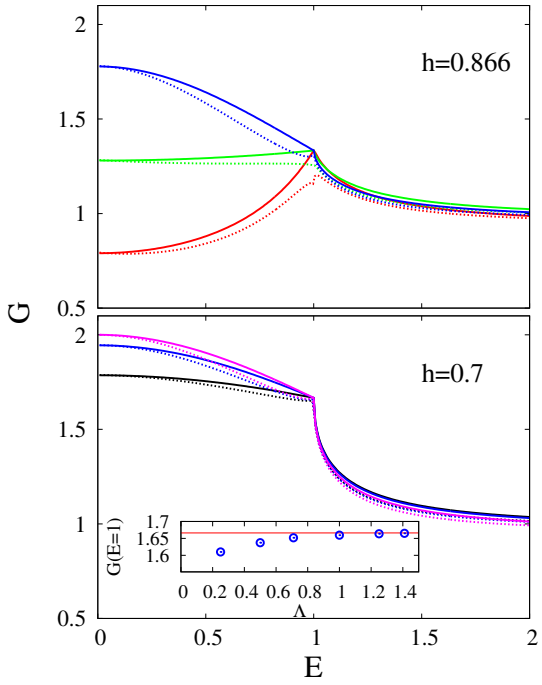

FIG. 2. (Color online) Bias dependence of the results for the forward conductance, G, in thick F-S bilayers (see text). The values of h are indicated. In both main panels the solid and dashed curves show G, in units of e^2/h for non-self-consistent and self-consistent results, respectively. The bias E is in units of the S bulk gap Δ_0. In the top panel the (red) lower curves are for a mismatch parameter $\Lambda = 0.25$, (green) the middle curves for $\Lambda = 0.5$, and the (blue) higher curves for $\Lambda = 1$. In the bottom panel, the (purple) top curves are for $\Lambda = 1.41$, the (blue) curves are as in the top panel, and the (black) lower ones for $\Lambda = 0.71$. The inset (see text) shows $G(E=1)$ vs. Λ in the self consistent calculation (dots) and the non-self-consistent result (line).

III. RESULTS

The forward scattering conductances G are computed by considering a particle incident with an angle $\theta_i \cong 0$ (normal incidence). Angular averaging has been discussed in the text above Eq. (23). The bias energy $E \equiv eV$ is in units of the zero temperature gap, Δ_0, in bulk S material and e^2/h is used as the natural unit of conductance. When the F_1 and F_2 regions are made of same F material, i.e., $h_1 = h_2$ and $k^\pm_{\uparrow 1,(\downarrow 1)} = k^\pm_{\uparrow 2,(\downarrow)2}$, we will use h (not to be confused with Planck's constant) and $k^\pm_{\uparrow,(\downarrow)}$ to denote their exchange fields and wavevectors. This is the case we will mostly study. All results are for the low-T limit. All of the lengths are measured in unit of k_{FS}^{-1} and denoted by capital letters, e.g. D_S denotes $k_{FS}d_S$.

A. Bilayers

We begin with a brief discussion of self-consistent results for the tunneling conductance in F-S bilayers, contrasting

them with non-self-consistent results. We assume that the S layer is very thick so that the pair amplitude saturates to its bulk value deep inside the S region. In this subsection, the dimensionless superconducting coherence length Ξ_0 is taken to be 50 and the thicknesses D_F and D_S of the F and S layers are both $15\Xi_0$. By computing the pair amplitudes via the direct diagonalization method,[24] we have verified that they indeed saturate to their bulk value with this large ratio of D_S to Ξ_0.

As discussed in Sec. I, the replacement of non-magnetic metals with ferromagnets in a bilayer leads to strong suppression of the Andreev reflection in the subgap region. The decrease of the zero bias conductance (ZBC) strongly depends on the magnitude of the exchange field in F. This dependence is used to measure the degree of spin-polarization of magnetic materials experimentally.[15,16] However, in early theoretical work,[12,13] it was shown that to accurately determine the degree of spin-polarization, one has to consider the Fermi wavevector mismatch (FWM), Λ, as well as the interfacial barriers. The ZBC peak is very sensitive to both spin-polarization and FWM and the dependence cannot be characterized by a single parameter.

We display in Fig. 2 forward conductance vs. bias results for both the self-consistent and non-self-consistent calculations, at two different values of the exchange fields and several FWM values. One sees at once that the self-consistent results approach the non-self-consistent ones in the zero bias limit, while deviating the most for energies near the superconducting gap. The ZBC decreases with increasing h and with decreasing Λ. Also, larger h indeed leads to a conspicuous reduction in the subgap conductance and so does the introduction of FWM. One can conclude that the behavior of the ZBC can not be characterized by only one parameter, either h or Λ. Instead, one should expand the fitting parameter space to determine the degree of spin polarization.

In the non-self-consistent framework, the conductance at the superconducting gap ($E = 1$ in our units) is independent of Λ at a given h. However, earlier work[49] predicted that this conclusion is invalid in self-consistent approach, and that the conductance at the superconducting gap varies monotonically with increasing Λ. Here we verify this via our self-consistent transfer matrix method. The inset in the bottom panel of Fig. 2 clearly shows this dependence on Λ. Figure 2 also shows that the self-consistent results (dashed curves) on subgap conductances are in general lower than those obtained in the non-self-consistent framework (solid curves) for a strong exchange field. On the other hand, in the high bias limit, the self-consistent results become similar to the non-self-consistent ones. This is simply because the particle does not experience much of a difference between a step-like pair potential and a smooth pair potential when it is incident with high enough energy. Finally, clear cusps appear at the superconducting gap value in some cases, e.g., the forward scattering conductance curve at $h = 0.866$ and $\Lambda = 1$. This is consistent with what is found in previous work[49] for thick bilayers.

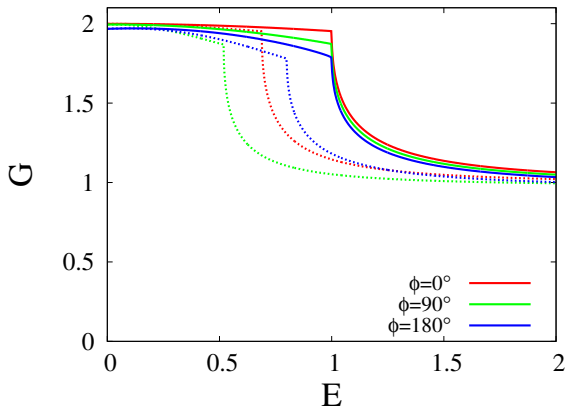

FIG. 3. (Color online) Comparison between the self-consistent and non-self-consistent forward scattering conductances of F_1F_2S trilayers. The solid and the dashed lines are for non-self-consistent and self-consistent results respectively. The (red) curves, highest at the critical bias (CB) are for $\phi = 0°$. The (blue) curves, lowest at CB, are for $\phi = 180°$. We have $D_{F1} = 10$, $D_{F2} = 12$, and $D_S = 180$ (see text).

B. Trilayers

We now discuss our results for F_1F_2S trilayers of finite widths. First, we discuss the dependence of the tunneling conductances on the angle ϕ between $\mathbf{h}_1$ and $\mathbf{h}_2$ (see below Eq. (2) and Fig. 1). An important reason for considering trilayers with finite widths is the strong dependence of the superconducting transition temperatures T_c on the angle ϕ due to proximity effects[39] and induced long-range triplet correlations.[58] Field induced switching effects[59] also make these structures attractive candidates for memory elements. The non-monotonic behavior of $T_c(\phi)$ with its minimum being near $\phi = 90°$, was extensively discussed in Ref. 39. This angular dependence has been shown to be related to the induced triplet pairing correlations[36]. The superconducting transition temperatures are also predicted to be positively correlated with the singlet pair amplitudes deep inside the S regions[39]. Therefore, it is of particular importance to consider systems of finite size to take into view the whole picture of proximity effects on the angular dependence of the tunneling conductance. For the results shown in this subsection, we assume the absence of FWM ($\Lambda = 1$).

1. *Forward Scattering*

As a typical example of our results, we show in Fig. 3 results for the ϕ dependence of the forward scattering conductances. The exchange field we use here for both F layers is $h = 0.3$, and the thicknesses of the F_1 and F_2 layers correspond to $D_{F1} = 10$ and $D_{F2} = 12$ respectively, while the S layer has width $D_S = 180 = 1.5\Xi_0$. Results obtained via the non-self-consistent approach are plotted for comparison. In the non-self-consistent framework where the single parame-

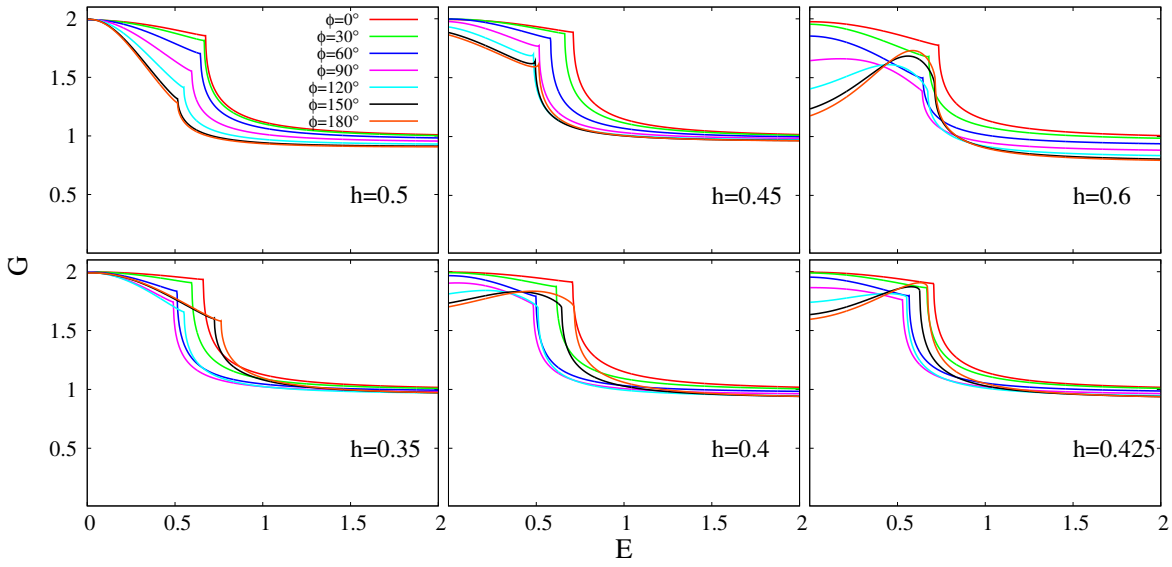

FIG. 4. (Color online) Forward scattering conductance of F_1F_2S trilayers for several angles ϕ as indicated in the legend. The top panels are for $D_{F1} = 10$, $D_{F2} = 12$, and $D_S = 180$ and the bottom panels for $D_{F1} = 10$, $D_{F2} = 18$, and $D_S = 180$. The exchange field strength h is indicated. For the left panels, the conductances at CB decrease with increasing ϕ. For the other panels, the ZBC (see text) decreases as ϕ increases.

ter Δ_0 describes the stepwise pair potential, one sees in Fig. 3 that for all values of the angle ϕ the conductance curves drop when the bias is at Δ_0, corresponding to $E = 1$ in our units. In contrast, for the self-consistent results, one can clearly see in Fig. 3, that the drop in the conductance curves occurs at different bias values for different angles. We also see that this critical bias (which we will denote by CB) depends on ϕ non-monotonically, with $\phi = 180°$ corresponding to the largest and $\phi = 90°$ to the smallest bias values. Since the CB depends on the strength of the superconducting gap deep inside the S regions, the non-monotonicity of the CB in Fig. 3 is correlated with the non-monotonicity of T_c. The CB never reaches unity, in these trilayers, due to their finite size. Accordingly, this feature of the correct self-consistent results implies that one cannot adequately determine the angular dependence of the forward conductance in the non-self-consistent framework. This feature also provides experimentalists with another way to measure the strength of the superconducting gap for different angles in these trilayers by determining the CB in a set of conductance curves. The remaining results shown in this section are all computed self-consistently.

In Fig. 4, we present more results for the dependence of the forward scattering conductances on ϕ. In the top panels the thicknesses of each layer and the coherence length are the same as Fig. 3. In the bottom panels we increase the thickness of the inner magnetic layer to $D_{F2} = 18$ while D_{F1}, D_S, and Ξ_0 remain unchanged. For each row of Fig. 4, results for three different exchange fields are plotted. In the top left panel ($h = 0.5$) we see that the angular dependence of the CB (or the magnitude of the saturated pair amplitudes) is monotonic with ϕ. Although this monotonicity is not common, we have verified that it is consistent with the theoretical results for $T_c(\phi)$ for the same particular case. The more usual non-monotonic dependence is found in all other panels, as discussed in the previous paragraph. In every case, we have also checked that the magnitude of the CB reflects the magnitude of the self-consistent pair amplitudes deep inside the superconductor.

For the ZBC, we see that the degree of its angular dependence is very sensitive to h. In the top left panel, with $h = 0.5$, the ZBC is nearly independent on ϕ. On the other hand, the ZBC in the top right panel, $h = 0.6$, drops by almost a factor of two as ϕ varies from the relative parallel (P) orientation, $\phi = 0°$, to the antiparallel (AP) orientation, $\phi = 180°$. This is a consequence of interference between the spin-up and spin-down wavefunctions under the influence of the rotated exchange field in the middle layer. In the top left panel, we see that the conductance at CB decreases with increasing angle. In other words, the zero bias conductance peak (ZBCP) becomes more prominent as ϕ is increased. However, for the top middle panel, $h = 0.45$, the development of the ZBCP is less noticeable when the angle ϕ is increased. In the top right panel, $h = 0.6$, the ZBCP evolves into a zero bias conductance dip (ZBCD) as ϕ varies from $\phi = 0°$ to $\phi = 180°$, with a clear finite bias conductance peak (FBCP) appearing just below the CB. This behavior is reminiscent[13] of that which occurs when a barrier, or mismatch, are present. In the bottom panels of this figure, corresponding to a larger value of D_{F2} one can observe similar features. For example, a slight change from $h = 0.35$ to $h = 0.4$ causes by itself a very large change in the behavior of the ZBC. Moreover, the evolution of the ZBCP to a ZBCD accompanies the occurrence of a FBCP when $\phi > 90°$. The location of the FBCP also moves closer to the CB value when ϕ increases. That these features of the ZBC depend on both the strength of exchange field (reflected in $k_{\uparrow}^{\pm}$ and $k_{\downarrow}^{\pm}$) and the thickness of the F_2 layer indicates that the ZBC shows the characteristics of a resonance scattering phenomenon as in an

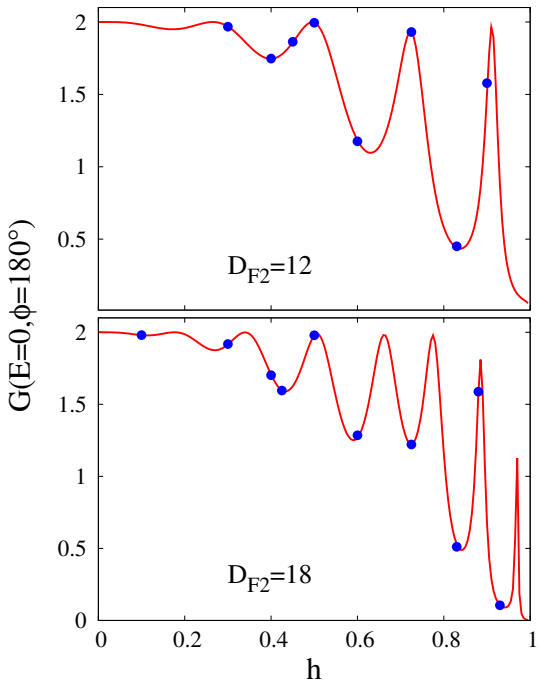

FIG. 5. (Color online) Resonance effects in the forward scattering conductance at zero bias for trilayers at $\phi = 180°$. In the top panel, the trilayers have same thicknesses as in the top panels of Fig. 4, and in the bottom panel, they are as in the bottom panels of Fig. 4.The (blue) dots are the results from our computations and the (red) curves from Eq. (33).

elementary quantum mechanical barrier. The main difference is that the scattering problem here involves the intricate interference between quasi-particle and quasi-hole spinors.

When the bias is high enough, the tunneling conductance approaches its normal state value. Thus, one can extract the magnetoresistance from the conductance at $E = 2$. We only discuss here the magnetoresistance's qualitative behavior. One can define a measure of the magnetoresistance as,

$$M_G(E,\phi) \equiv \frac{G(E,\phi = 0°) - G(E,\phi)}{G(E,\phi = 0°)}. \tag{32}$$

For all results shown in the panels of Fig. 4, the conductance at $E = 2$ decreases with increasing ϕ, i.e., it is a monotonic function of ϕ, the standard behavior for conventional, non-superconducting, spin-valves. Furthermore, one can also see that $M_G(E = 2, \phi = 180°)$ increases with exchange field. Therefore, the behavior of the magnetoresistance at large bias is as one would expect in the present self-consistent BTK framework. However, the behavior of $M_G(E = 0, \phi = 180°)$ that is associated with the behavior of the ZBC is generally a non-monotonic function of h.

We next investigate the high sensitivity of the ZBC to h by examining its resonances for two different F widths arranged in an AP magnetic configuration ($\phi = 180°$). To do so, we performed an analytic calculation of the ZBC in the non-self-consistent framework in situations where (as discussed in connection with Fig. 3) the results nearly coincide with those of self-consistent calculations. We find that the ZBC at $\phi = 180°$, $G(E = 0, \phi = 180°) \equiv G_{ZB}$, for a given h and D_{F2} is:

$$G_{ZB} = \frac{32 k_\uparrow^3 k_\downarrow^3}{A + 2\left(h^4 - 2h^2 - 2h^2 k_\uparrow k_\downarrow\right)\cos\left[2\left(k_\uparrow - k_\downarrow\right) D_{F2}\right]}. \tag{33}$$

The expression for A in Eq. (33) is:

$$a_1 \sin^2\left[\left(k_\uparrow + k_\downarrow\right) D_{F2}\right] + a_2\left[\cos\left(2k_\uparrow D_{F2}\right) - \cos\left(2k_\downarrow D_{F2}\right)\right] + a_3, \tag{34}$$

where $a_1 = 4h^2(1 - k_\uparrow k_\downarrow)^2$, $a_2 = 4h^3$, and $a_3 = h^4 + (-2 + h^2 - 2k_\uparrow k_\downarrow)^2$. Here we have omitted the $\pm$ indices for the quasi-particle and quasi-hole wavevectors, since we are in the zero bias limit. In Fig. 5, we plot Eq. (33) as a function of h for $D_{F2} = 12$ (top panel) and 18 (bottom panel). In this zero bias limit, the (blue) circles (self-consistent numerical results) are on top of the (red) curves (analytic results). As the thickness of the intermediate layer increases, the number of resonance maxima and minima increases. Therefore, the resonance behavior of the ZBC is more sensitive to h for larger D_{F2}, as we have seen in Fig. 4. For a given D_{F2}, the ZBC drops considerably as ϕ varies from $\phi = 0°$ to $\phi = 180°$ when h is near the minimum of the resonance curve (rightmost panels of Fig. 4). On the other hand, when h is near the resonance maximum (leftmost panels of Fig. 4), the ZBC is a very weak function of ϕ provided that h is not too strong. By examining the denominator of Eq. (33), we find that the terms involved in A are less important than the last term. This is because the wavelength $(k_\uparrow - k_\downarrow)^{-1}$ associated with that term is the dominant characteristic wavelength in the theory of proximity effects in F-S structures.[3,5] In both panels of Fig. 5, we see that the ZBC for $\phi = 180°$ vanishes in the half-metallic limit. To show this analytically, one can use the conservation of probability currents and write down the relation, valid when the bias is smaller than the superconducting gap:

$$\frac{k_{\uparrow 1}^-}{k_{\sigma 1}^+}|a_\uparrow|^2 + \frac{k_{\downarrow 1}^-}{k_{\sigma 1}^+}|a_\downarrow|^2 + \frac{k_{\uparrow 1}^+}{k_{\sigma 1}^+}|b_\uparrow|^2 + \frac{k_{\downarrow 1}^+}{k_{\sigma 1}^+}|b_\downarrow|^2 = 1. \tag{35}$$

By combining Eq. (35) with Eq. (22), it becomes clear that the subgap conductances arise largely from Andreev reflection. In the half-metallic limit, conventional Andreev reflection is forbidden due to the absence of an opposite-spin band: this leads to zero ZBC at $\phi = 180°$. Same-spin Andreev reflection (see discussion in the paragraph above Eq. (4)) is not allowed in collinear magnetic configurations. Equation (35) also reflects another important feature of the ZBC: the contributions to G at zero bias from the spin-up and down channels are identical except for the weight factor P_σ: one can prove analytically that the sum of first two terms (related to Andreev reflection) in Eq. (35) is spin-independent. As a result, the sum of last two terms, related to ordinary reflection, is also spin-independent, and so is the ZBC.

We briefly consider here one example where the two F materials in the trilayers have different field strengths. In this example all the thicknesses and the coherence length are as in the top panels of Fig. 4. In Fig. 6, we plot the forward scattering conductance for several ϕ at $h_1 = 0.6$ and $h_2 = 0.1$. One

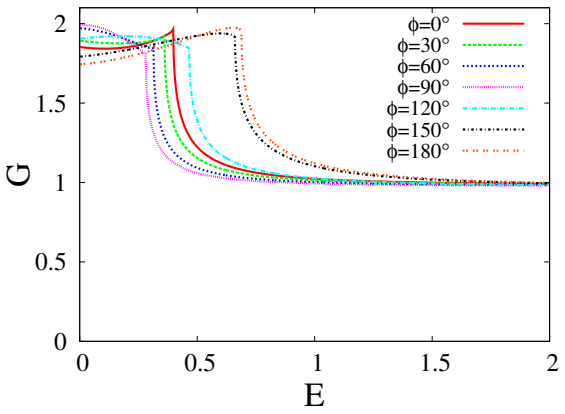

FIG. 6. (Color online) Forward scattering conductance of a F_1F_2S trilayer with differing magnetic materials corresponding to exchange fields of $h_1 = 0.6$ and $h_2 = 0.1$. Various magnetic orientations, ϕ, are considered as shown. Geometry and other parameters are as in the top panels of Fig. 4.

can quickly identify that the ZBC here is a non-monotonic function of ϕ with it maximum at the orthogonal relative magnetization angle, $\phi = 90°$. In contrast, results at equal exchange field strengths usually demonstrate monotonic behavior, as previously shown. However, many features are still the same, such as the formation of a FBCP when $\phi > 90°$. For $\phi = 0°$ and $\phi = 30°$, the conductance curves are not monotonically decreasing, as was the case at $h_1 = h_2$. There, when $h_1 = h_2$ and $\phi < 90°$, we always see monotonically decreasing behavior because the scattering effect due to misoriented magnetizations is not as great as at $\phi > 90°$. Also, when $h_1 \neq h_2$, we have to include in our considerations another scattering effect that comes from the mismatch between $k^{\pm}_{\uparrow 1,(\downarrow 1)}$ and $k^{\pm}_{\uparrow 2,(\downarrow 2)}$. Specifically, when $\phi = 0°$, the only important scattering effect is that due to mismatch from $h_1 \neq h_2$ and it leads to suppression of the ZBC at $\phi = 0°$. However, we see that the scattering due to the misoriented magnetic configuration ($\phi \neq 0°$) compensates the effect of mismatch from $h_1 \neq h_2$ and ZBC is maximized when $\phi = 90°$. Qualitatively, one can examine Eqs. (8) and (9) and verify that the spinor at $\phi = 90°$ is composed of both pure spin-up and spin-down spinors with equal weight, apart from phase factors. As a result, the scattering effect due to mismatch from $k^{\pm}_{\uparrow 1,(\downarrow 1)}$ and $k^{\pm}_{\uparrow 2,(\downarrow 2)}$ is reduced. We also verified that, when the strength of h_2 is increased towards h_1, the locations for the maximum of the ZBC(ϕ) curves gradually move from $\phi = 90°$ at $h_2 = 0.1$ to $\phi = 0°$ at $h_2 = 0.6$.

2. *Angularly averaged conductance*

We now present results for the angularly averaged conductance, $\langle G\rangle$ as defined in Eq. (23). The details of the angular averaging are explained under Eq. (25). The angularly averaged conductance is relevant to a much wider range of experimental results than the forward conductance, which is relevant strictly only for some point contact experiments. This is particularly true if one recalls that the critical angle $\theta_{c\sigma}$ and the weight factor for angular averaging in Eq. (23) used in this work can be modified based on a real experimental set-up or on the geometry of the junction.

In Fig. 7, we present results for $\langle G\rangle$ at $D_{F2} = 12$ (left panels) and $D_{F2} = 18$ (right panels). All curves are obtained with $D_{F1} = 10$ and $D_S = 180 = 1.5\Xi_0$ at the values of h indicated in each panel. Results are plotted over the entire range of ϕ values. The CB values obtained for $\langle G\rangle$ are again non-monotonic functions of ϕ and the non-monotonicity matches that of the saturated pair amplitudes, for the reasons previously given. The CB values for $\langle G\rangle$ in these cases are the same as those for the forward scattering conductance. One can also see that the resonance phenomenon is washed out in the angularly averaged conductance. For example, the resonance curve in the top panel of Fig. 5 tells us that $h \approx 0.3$ and $h \approx 0.6$ correspond respectively to a resonance maximum and minimum of the ZBC in the forward scattering G. However, in the top left panel of Fig. 7, the ZBC is no longer a weak function of ϕ and it gradually decreases when ϕ is increased. Near the resonance minimum, $h = 0.6$, bottom left panel of Fig. 7, we can see a trace of the appearance of the FBCP when ϕ is above 90°. This FBCP in $\langle G\rangle$ is not as prominent as that in the forward scattering G, due to the averaging.

The magnetoresistance measure $M_G(E = 2, \phi)$ is larger for $\langle G\rangle$ than for the forward scattering conductance. For example, $M_G(E = 2, \phi = 180°)$ in the forward scattering conductance for $h = 0.6$ and $D_{F2} = 12$ is half of that in $\langle G\rangle$. As for the zero bias magnetoresistance $M_G(E = 0, \phi = 180°)$ in $\langle G\rangle$, it is of about the same order as $M_G(E = 2, \phi = 180°)$ and it does not depend on where it is located in the resonance curve, Fig. 5 (recall that $M_G(E = 0, \phi = 180°)$ for the forward scattering conductance almost vanishes at the resonance maximum).

In the right panels of Fig. 7, we plot results for a larger D_{F2} with values of $h = 0.35$ (near a resonance maximum) and $h = 0.725$ (near a resonance minimum). They share very similar features with the thinner D_{F2} case in the left panels. However, for $h = 0.725$, we see that the ZBC values at different ϕ shrink to almost or less than unity and they are just barely higher than the conductance at $E = 2$ because the contributions from Andreev reflection are strongly suppressed in such a high exchange field. Another important feature in the angularly averaged results for higher exchange fields (bottom panels in Fig. 7) is the existence of cusps at the CB. To understand the formation of these cusps, we analyze $\langle G\rangle$ by dividing the contribution from all angles into two ranges: the range above and the range below the conventional Andreev critical angles θ^A_c [see discussion below Eq. (26)]. Consider e.g., the case of spin-up incident quasi-particles. When $\theta^A_c \equiv \sin^{-1}[\sqrt{(1-h)/(1+h)}] < \theta_i < \sin^{-1}[\sqrt{1/(1+h)}]$, the conventional Andreev reflected waves become evanescent while the transmitted waves are still traveling waves above the CB. When $\theta_i > \sin^{-1}[\sqrt{1/(1+h)}]$, both the conventional Andreev reflected waves and the transmitted waves become evanescent. Here, $\theta_{c\uparrow} = \sin^{-1}[\sqrt{1/(1+h)}]$ is the upper limit in Eq. (23).

The case of spin-down incident quasi-particles is trivial, because the dimensionless incident momentum is $\sqrt{1-h}$ which is less than both the conventional Andreev reflected wavevec-

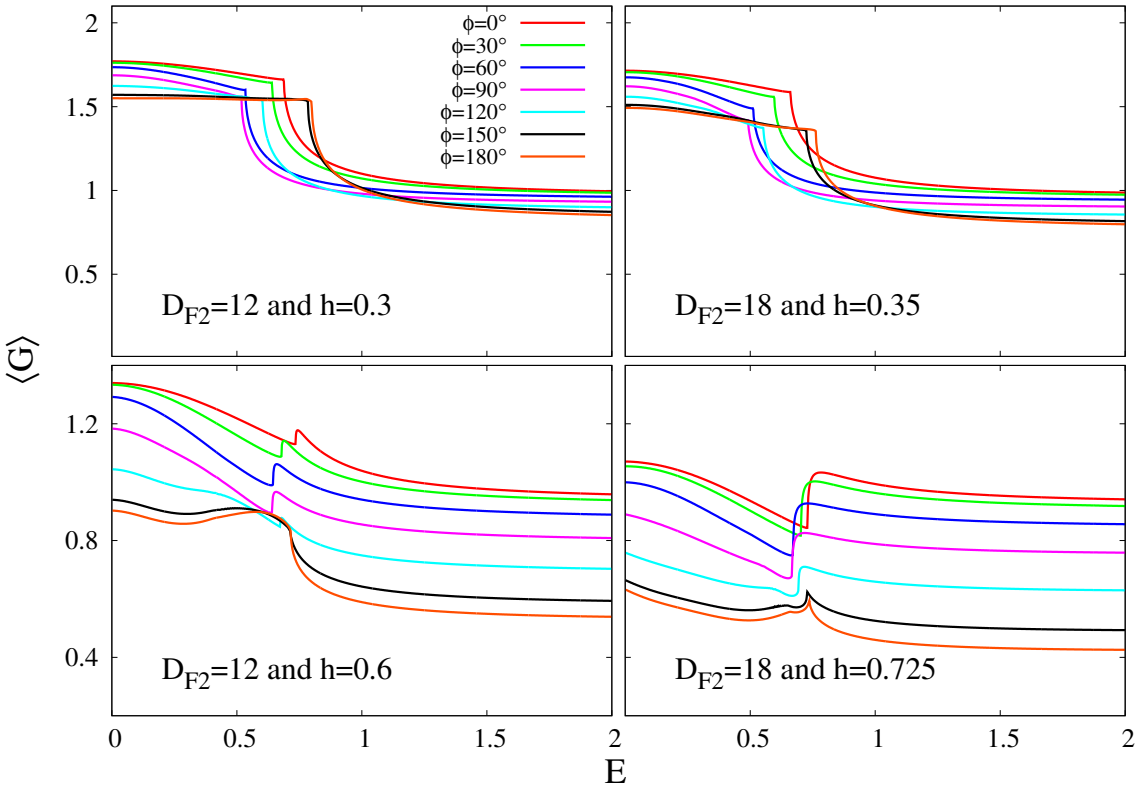

FIG. 7. (Color online) Bias dependence of the angularly averaged conductance of F_1F_2S trilayers for several angles ϕ (see legend). In the left panels, $D_{F1} = 10$,and $D_S = 180 = 1.5\Xi_0$, as in the top panels of Fig. 4. In the right panels, $D_{F1} = 10$ as in the bottom panels of Fig. 4. In all cases, the ZBC decreases with increasing ϕ.

tor, $\sqrt{1+h}$, and the transmitted wavevector, (unity in our conventions). Therefore, all the reflected and transmitted waves above the CB are traveling waves. As a result, we should consider all possible incident angles and the upper limit of Eq. (23) is $\pi/2$. Let us therefore focus on the nontrivial spin-up component of $\langle G\rangle$. In Fig. 8 we separately plot the contributions to $\langle G_\uparrow\rangle$ from angles in the range above θ_c^A (top panels) and below (bottom panels) for the field values and geometry in the left panels of Fig. 7, in particular $D_{F2} = 12$. These contributions we will denote as $\langle G_\uparrow(E)\rangle_{above}$ and $\langle G_\uparrow(E)\rangle_{below}$ respectively. The $\langle G_\uparrow(E)\rangle_{below}$ contributions, in the bottom panels of Fig. 8 are, for both $h = 0.3$ and $h = 0.6$, similar to the result for their total forward scattering counterpart (see Fig. 3 and the top right panel of Fig. 4). Of course, the angular averaging leads to a smearing of the pronounced features originally in the forward scattering G. Qualitatively, the similarity comes from the propagating nature of all possible waves except the transmitted waves below the CB when $\theta_i < \theta_c^A$. Therefore, the forward scattering G is just a special example with the incident angle perpendicular to the interface.

In the subgap region, the contribution to $\langle G_\uparrow(E)\rangle_{above}$ is vanishingly small although small humps appear when the exchange fields in the two F layers are non-collinear, i.e., $\phi \neq 0, \pi$. These small humps are generated by the process of anomalous, equal-spin Andreev reflection. This process is possible in trilayers because, in a non-collinear magnetic configuration, a spin up quasiparticle can Andreev reflect as a spin-up hole. This can be seen from the matrix form of the BdG equations, Eq. (2). The occurrence of anomalous Andreev reflection leads to some important physics which we shall discuss in the next sub-subsection. One can see from Fig. 8, that when the exchange fields are strictly parallel or anti-parallel to each other, anomalous Andreev reflection does not arise.

Above θ_c^A, the conventional Andreev-reflected wave is evanescent and it does not contribute to $\langle G_\uparrow\rangle$. When the bias is above the saturated pair amplitude, contributions to $\langle G_\uparrow\rangle$ from the upper range are provided by both the transmitted waves and by anomalous Andreev reflected waves. Recall that ordinary transmitted waves are propagating when E is greater than the saturated pair amplitudes. We also see that $\langle G_\uparrow\rangle_{above}$ decreases with increasing ϕ. At $\phi = 180°$, $\langle G_\uparrow\rangle$ is vanishingly small due to the effect of a large mismatch from the anti-parallel exchange field. Note also that the contribution from above θ_c^A is less in the $h = 0.3$ case than at $h = 0.6$. This is mainly due to a smaller fraction of states at $h = 0.3$ with incident angles larger than θ_c^A. On the other hand, the contribution from below θ_c^A is larger in the $h = 0.3$ case. The in-

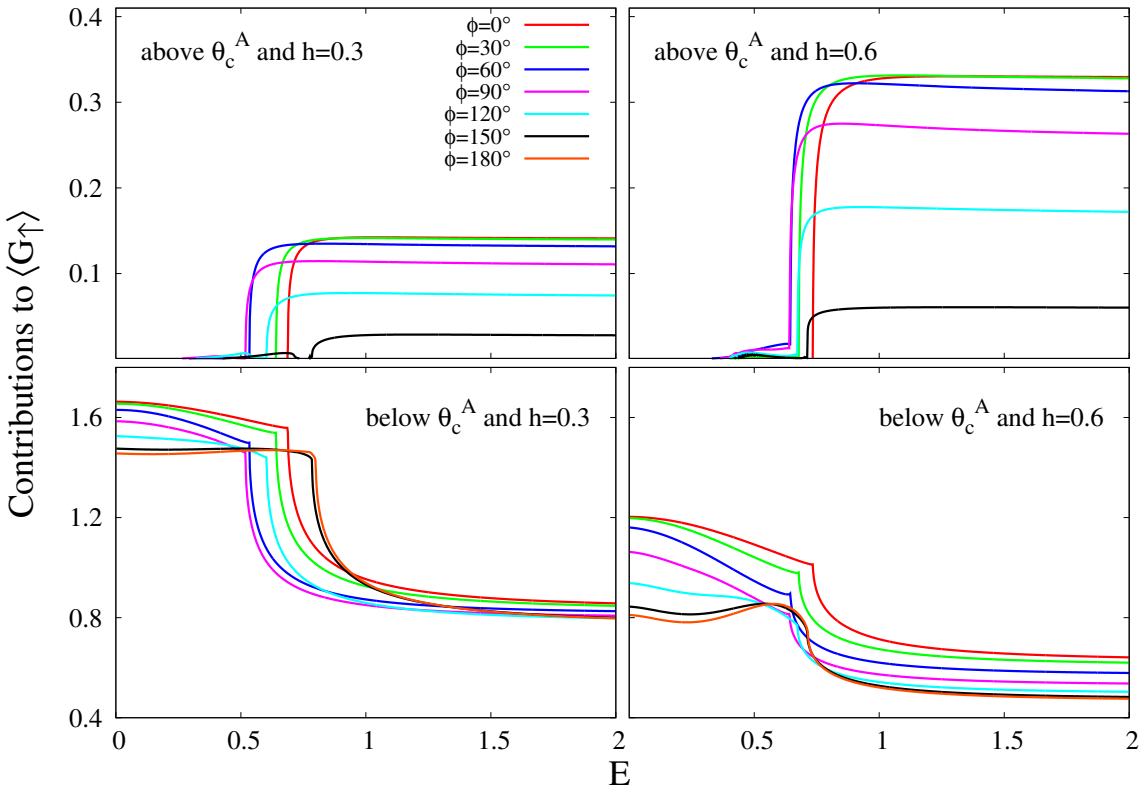

FIG. 8. (Color online) Contributions (see text) to the spin-up angularly averaged conductance, $\langle G_\uparrow \rangle$, from angular ranges above (top panels) and below (bottom panels) the Andreev critical angle θ_c^A. Several values of ϕ are considered, as indicated. The top panel results at $\phi = 180°$ are vanishingly small. The geometric and exchange field values are as in the left panels of Fig. 7. For the top panels, the plotted values at $E = 2$ decrease with increasing ϕ. For the bottom panels, their values at both $E = 0$ and $E = 2$ decrease with increasing ϕ.

crease of $\langle G_\uparrow \rangle_{above}$ and the decrease of $\langle G_\uparrow \rangle_{below}$ from $h = 0.3$ to $h = 0.6$ gives rise to the cusp at the CB, when adding these two contributions together.

3. *Anomalous Andreev reflection*

As we have seen, equal-spin (anomalous) Andreev reflection (ESAR) can be generated when the magnetic configuration is non-collinear. We have previously shown that conventional Andreev reflection is forbidden when $\theta_i > \theta_c^A = \sin^{-1}(\sqrt{(1-h_1)/(1+h_1)})$. Thus, θ_c^A vanishes in the half-metallic limit. In that case, conventional Andreev reflection is not allowed for any incident angle θ_i and the subgap $\langle G_\uparrow \rangle$ arises only from ESAR. For this reason, in this sub-subsection we present results for a trilayer structure that consists of one half-metal ($h_1 = 1$) and a much weaker ($h_2 = 0.1$) ferromagnet. The weaker ferromagnet serves the purpose of generating ESAR. A somewhat similar example that has been extensively discussed in the literature is that of half metal-superconductor bilayers with spin-flip interface.[32,33,60,61] There the spin-flip interface plays the same role as the weaker ferromagnet here. Another interesting phenomenon also related to ESAR is the induction of triplet pairing correlations in F-S structures.[24,30,34,39] To induce this type of triplet pairing, F-S systems must be in a non-collinear magnetic configuration such as F_1F_2S or F_1SF_2 trilayers with $\phi \neq 0, \pi$. Hence, the mechanism behind induced triplet pairing correlations is also responsible for ESAR and these two phenomena are closely related.

In Fig. 9, we plot the $\langle G \rangle$ of this particular system for several ϕ. The geometrical parameters are again $D_{F1} = 10$, $D_{F2} = 12$, and $D_S = 180$. We have $\langle G \rangle = \langle G_\uparrow \rangle$ because the weight factor $P_\downarrow = 0$ in this half metallic case. For $\phi = 0°$ and $\phi = 180°$ the CB value is about 0.65 and, below the CB (in the subgap region), $\langle G \rangle$ vanishes because the conventional Andreev reflection is completely suppressed and ESAR is not allowed in the collinear cases. For $\phi = 30°$ and $\phi = 150°$, the CB is near 0.4 and 0.5 respectively and all of the subgap $\langle G \rangle$ is due to ESAR. The CB values for $\phi = 60°$, 90°, and 120° are 0.15, 0.12, and 0.15. For these three angles, a FBCP clearly forms, arising from the ESAR in the subgap region.

To examine the conductance in the subgap region, which is in this case due only to ESAR, we choose the $\phi = 150°$ angle and plot, in Fig. 10, the contributions to G (for this case G and $\langle G \rangle$ are very similar) from the reflected spin-up particle and the reflected spin-up hole wavefunctions. The spin-down particle and spin-down hole wavefunctions are evanescent and

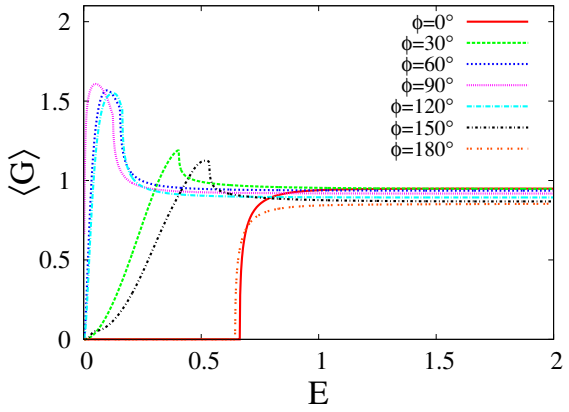

FIG. 9. (Color online) The angularly averaged conductance of F_1F_2S trilayers with exchange field $h_1 = 1$ and $h_2 = 0.1$ for several values of ϕ. See text for discussion.

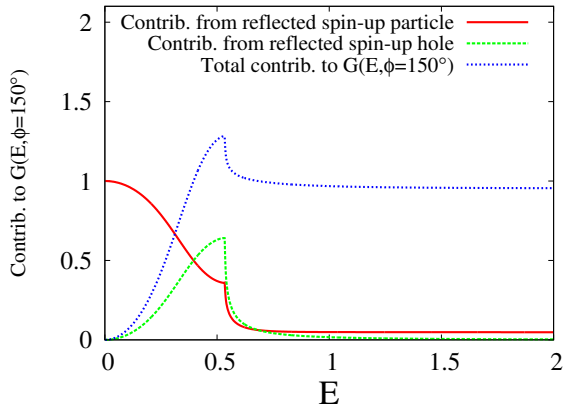

FIG. 10. (Color online) Contributions to $G(E, \phi = 150°)$, computed for the parameter values used in Fig. 9, from the spin-up quasiparticle and spin-up quasihole ESAR (see text for discussion). The total G is also shown.

do not contribute to the conductance. Thus, Eq. (22) reads $G = 1 + (k^-_{\uparrow 1}/k^+_{\uparrow 1})|a_\uparrow|^2 - |b_\uparrow|^2$. The quantities plotted are the second ((green) curve) and third ((red) curve, highest at the origin) terms in this expression. The value of G is also plotted. One sees that the reflected ESAR amplitudes decay very quickly above the CB. However, these reflected amplitudes are quite appreciable in the subgap region. In other words, the supercurrent in the subgap region contains signatures of the triplet correlations. This confirms the simple picture[9] that above the CB the current flowing throughout the junction is governed by the transport of quasiparticles. However, below the CB it is dominated by ESAR.

4. *Spin current densities and spin-transfer torques*

Finally, we now report on spin-dependent transport quantities, including the spin current, the spin-transfer torques, and their connections to the local magnetization at finite bias.

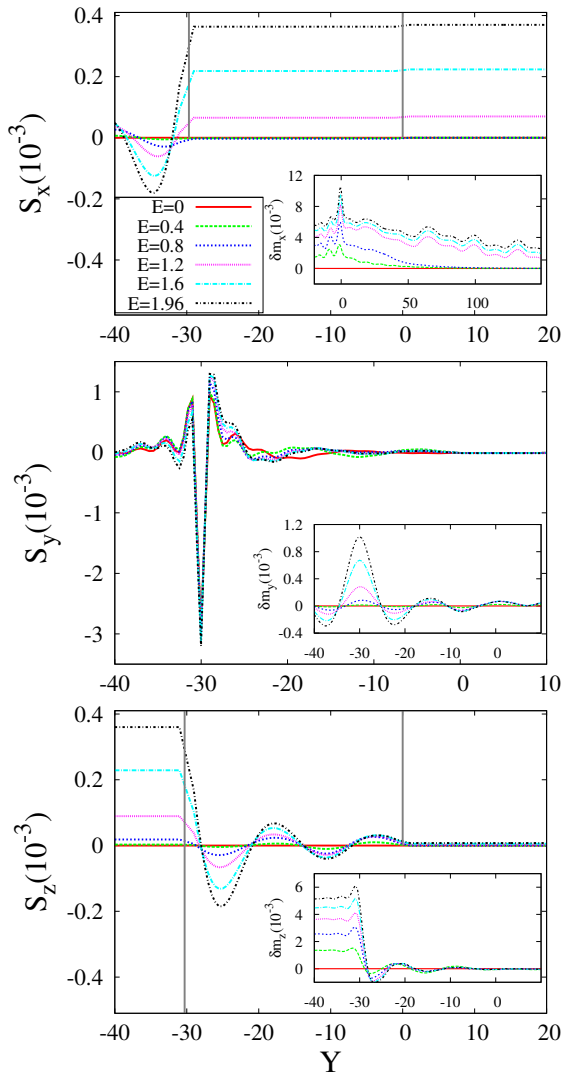

FIG. 11. (Color online) The components of the spin current density, S_x, S_y, and S_z, calculated from Eq. (31) are plotted vs. $Y \equiv k_F y$ for several values of the bias $E \equiv eV$ (main panels). We have $\phi = 90°$, $h = 0.1$, $D_{F1} = 250$, $D_{F2} = 30$, $D_S = 250 = 5\Xi_0$. The F_2-S interface is at $Y = 0$ and the F_1-F_2 interface at $Y = -30$. Vertical lines at these interfaces in the top and bottom panels help locate the different regions. Only the central portion of the Y range is included (see text). The ranges included depend on the component. The insets show the change in each component of the local magnetization, $\delta\mathbf{m}(E) \equiv \mathbf{m}(E) - \mathbf{m}(0)$, also as a function of Y. The values of E are as in the main plot, the ranges included may be different.

An objective here is to demonstrate that the conservation law Eq. (27) which in the steady state is simply:

$$\frac{\partial}{\partial y} S_i = \tau_i, \quad i = x, y, z, \tag{36}$$

is satisfied in our self consistent calculations for F_1F_2S trilayers. We consider these spin dependent quantities in a trilayer with $h = 0.1$ and a non-collinear orthogonal magnetic config-

uration, $\phi = 90°$. Thus, the internal field in the outer electrode F_1 is along the z axis, while that in F_2 is along x. The thicknesses are $D_{F1} = 250$, $D_{F2} = 30$, and $D_S = 250 = 5\Xi_0$.

A set of results is shown in Fig. 11. There, in the three main plots, we display the three components of the spin current density, computed from Eqs. (31) and normalized as explained below that equation. They are plotted as functions of the dimensionless position $Y \equiv k_F y$ for several values of the bias V, $E \equiv eV$. The F_2-S interface and the F_1-F_2 interface are located at $Y = 0$ and $Y = -30$, respectively. For clarity, only the range of Y corresponding to the "central" region near the interfaces is included in these plots: the shape of the curves deeper into S or F_1 can be easily inferred by extrapolation. From these main panels, one sees that the current is spin-polarized in the x-direction (the direction of the exchange field in F_2) to the right of F_1-F_2 interface, including the S region. Furthermore, S_x is found to be a constant except in the F_1 region, where it exhibits oscillatory behavior. This indicates the existence of a non-vanishing, oscillating spin-transfer torque in the F_1 layer, as we will verify below. We also see that S_x vanishes when the bias is less than the superconducting gap in bulk S ($E < 1$ in our notation). In fact, the behavior of S_x with V is similar to that of the ordinary charge current in an N-S tunneling junction with a very strong barrier where there is no current until $V > \Delta_0$. This phenomenon is very different from what occurs in ordinary spin valves (F_1-F_2), where the spin current is not blocked below any finite characteristic bias.

The S_y component, along the normal to the layers, is shown in the middle main panel of Fig. 11. It depends extremely weakly on the bias E. It is very small except near the interface between the two ferromagnets but there it is about an order of magnitude larger than the other two components. Hence only a somewhat smaller Y range is shown. Unlike the S_x and S_z components, S_y does not vanish even when there is no bias applied to the trilayer (the (red) curve in this panel). From these observations, one can infer that S_y is largely derived from its static part with only a very small contribution from the effect of finite bias. The emergence of a static spin current is due to the leakage of the local magnetization m_z into the F_2 layer and of m_x into the F_1 layer. This explains why the static spin current S_y is mostly localized near the F_1-F_2 interface. The S_z component (lower panel) is constant in the F_1 region, as one would expect. It oscillates in the F_2 region, and vanishes in the S layer. As opposed to the S_x component, S_z is non-vanishing, although very small, when $E < 1$ It increases rapidly with bias when $E > 1$. The oscillatory behavior of S_z, again, is related to the local spin-transfer torque as we will verify below.

We can summarize the behavior of the spin current vector, in this $\phi = 90°$ configuration, as follows: when $E > 1$, the spin current, which is initially (at the left side) spin-polarized in the $+z$ direction, is twisted to the x direction under the action of the spin torques discussed below, as it passes through the second magnet, which therefore acts as a spin filter. The current remains then with its spin polarization in the $+x$ direction as it flows through the superconductor. Thus in this range of E the trilayer switches the polarization of the spin current. On the other hand, when $E < 1$, the small z-direction spin-polarized current tunneling into the superconductor is gradually converted into supercurrent and becomes spin-unpolarized.

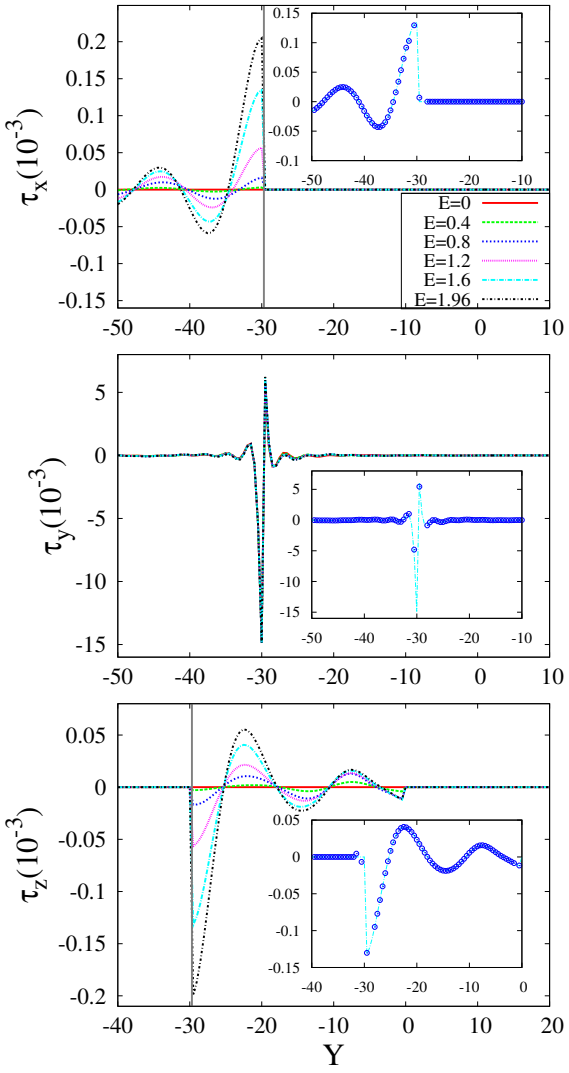

FIG. 12. (Color online) The components of the spin-transfer torque $\boldsymbol{\tau} \equiv 2\mathbf{m} \times \mathbf{h}$ plotted vs. Y for several bias values. All parameters and geometry are as in Fig. 11. Vertical lines, denoting interfaces, are in the top and bottom panels. The insets show (for bias $E = 1.6$) the torque ((blue) dashed line) and the derivative of the component of spin current density ((blue) circles). The lines and circles agree, proving that Eq. (36) holds.

In the insets of the three panels of Fig. 11, we illustrate the behavior with bias of the corresponding component of the local magnetization as it is carried into S. Specifically, we plot the components of the vector difference between the local magnetization with and without bias, $\delta\mathbf{m}(E) \equiv \mathbf{m}(E) - \mathbf{m}(E = 0)$, as a function of Y. The range of Y is chosen to display the salient aspects of the behavior of this quantity, and it is not the same as in the main plots, nor is it the same for each component. The bias values are the same as in the main plots, however. The magnetizations are computed from Eqs. (29) and normalized in the usual way, as discussed below Eqs. (31).

In these units, and at $h = 0.1$ the value of the dominant component of $\mathbf{m}$ in the magnetic layers is about 0.15. This scale should be kept in mind.

The behavior of the x component is nontrivial in the F_2 and S regions, and the corresponding Y range is included in the top panel inset. When the applied bias is below the bulk S gap value, $\delta m_x(E)$ penetrates into the S layer with a decay length $\sim \Xi_0 = 50$. This decay length is much longer than that found for the static magnetization, $\mathbf{m}(0)$.[39] When the bias is above the gap, $\delta m_x(E)$ penetrates even more deeply into the S layer, with a clearly very different behavior than for $E < 1$. This long-range propagation is of course consistent with the behavior of S_x, as S_x, the spin current polarized in the x direction, appears only when $E > 1$. The magnitude of δm_y is much smaller than that of δm_x or δm_z. It peaks near the F_1-F_2 interface and that range of Y is emphasized in the middle inset. Its overall scale monotonically increases with increasing bias. It damps away from the interface in an oscillatory manner. As to δm_z, which can conveniently be plotted in the same Y range, it decays with a very short decay length and oscillates in F_2. The overall damped oscillatory behavior of δm_y and δm_z in the F_2 region reflects the precession, as a function of position, of the spin density around the local exchange field that points toward the $+x$ direction. This phenomenon is well known in spin-valves.[62] The oscillation periods for δm_y, δm_z, S_x, and S_z are very similar and of the order of $1/(hk_{FS})$.

Next, we investigate the spin-transfer torque, $\boldsymbol{\tau} \equiv 2\mathbf{m} \times \mathbf{h}$. This quantity, computed from the normalized values of h and $\mathbf{m}$, is plotted as a function of position in Fig. 12 for the same system as in Fig. 11. Results are shown for each of its three components in the main panels of the figure. One sees that at zero bias, $E = 0$, both τ_x and τ_z vanish identically. In the F_1 layer, τ_x increases in magnitude with increasing E. It vanishes in F_2 and in S. The behavior of τ_z is, as one would expect, the converse: it vanishes in F_1 and S, and its magnitude increases in F_2. The oscillatory behavior of τ_x and τ_z is consistent, as we shall see below, with the results for S_x and S_y. The component normal to the layers, τ_y, is nonvanishing only near the F_1-F_2 interface, although its peak there attains a rather high value, nearly two orders of magnitude larger than the peak value of the other components. It is independent of bias, consistent with the behavior of S_y.

In the insets, we verify, for each component, that Eq. (36) is satisfied, that is, that our self-consistent methods strictly preserve the conservation laws in this nontrivial case. (We have already mentioned that we have verified that the charge or particle current are independent of y). We specifically consider the bias value $E = 1.6$ as an illustration. Consider first the top panel inset. There we plot both the x component of the spin-transfer torque, τ_x (blue dashes), taken from the corresponding main plot, and the derivative of the spin current, $\partial S_x/\partial Y$ (blue circles), obtained by numerically differentiating the corresponding result in the top panel of Fig. 11. Clearly, the curves are in perfect agreement. (One can easily check that with the normalizations and units chosen there should be no numerical factor between the two quantities). In the second panel, the same procedure is performed for the y component, although in this case, because of the very weak dependence of both S_y and τ_y on bias, the value of the latter is hardly relevant. Nevertheless, despite the evident difficulty in computing the numerical derivative of the very sharply peaked S_y, the agreement is excellent. For τ_z, its vanishing in the F_1 region is in agreement with the constant spin current in that layer. The conservation law Eq. (36) is verified in the inset for this component, again at bias $E = 1.6$. Just as for the x component, the dots and the line are on top of each other. Thus the conservation law for each component is shown to be perfectly obeyed.

The results of this sub-subsection can be summarized as follows: the finite bias leads to spin currents. As opposed to the ordinary charge currents, these spin currents are generally not conserved locally because of the presence of the spin-transfer torques which act as source terms and are responsible for the change of spin-density. But a self-consistent calculation *must* still contain exactly the correct amount of non-conservation, that is, Eq.(36) must be satisfied. It is therefore of fundamental importance to verify that it is, as we have.

IV. CONCLUSIONS

In summary, we have investigated important transport properties of F_1F_2S trilayers, including tunneling conductances and spin transport. To properly take into account the proximity effects that lead to a spatially varying pair potential, we have incorporated a transfer matrix method into the BTK formalism. This allows us to use self-consistent solutions of the BdG equations. This technique also enables us to compute spin transport quantities including spin transfer torque and spin currents. We have shown that in F-S bilayers the self-consistent calculations lead to conductances at the superconducting gap that increase with the Fermi wavevector mismatch whereas non-self-consistent ones predict they are insensitive to this parameter. In F_1F_2S trilayers, we have found that the critical bias CB (where tunneling conductance curves drop) for different relative magnetization angles, ϕ, depends on the strength of the superconducting order parameter near the interface. The angular dependence of the critical bias reflects that of the transition temperatures T_c, which are usually nonmonotonic functions of ϕ. For forward scattering in these F_1F_2S trilayers, we found that the dependence of the zero bias conductance peak (ZBCP) on ϕ is related to both the strength of the exchange fields and the thickness of the F_2 layers. This remarkable behavior can be explained via quantum interference effects. At the resonance minimum, the ZBCP drops significantly and monotonically from $\phi = 0^\circ$ to $\phi = 180^\circ$. On the other hand, the ϕ dependence of the ZBCP is very weak when it is at its resonance maximum. For asymmetric cases where $h_1 \neq h_2$, we found that the ZBCP is a nonmonotonic function of ϕ with its value at $\phi = \pi/2$ being the maximum. We have also investigated the angularly averaged tunneling conductances, $\langle G \rangle$, and found that features of resonance effects are then somewhat washed out due to the averaging. However, by studying $\langle G \rangle$ in the subgap regions, we found that anomalous (equal spin) Andreev reflection (ESAR) arises when ϕ corresponds to noncollinear orientations. The emergence of

ESAR is correlated with the well-known induced triplet pairing correlations in proximity coupled F-S structures. When the outer magnet is a half metal, the $\langle G \rangle$ signatures arise chiefly from the process of ESAR. We have also studied the bias dependence of the spin currents and spin transfer torques and their general behavior in F_1F_2S trilayers with $\phi = 90^\circ$ (the exchange fields in F_1 and F_2 point toward the z and x directions, respectively). The spin current components are in general non-conserved quantities. The S_z component, parallel to the local exchange field in the F_1 layer, does not change in the F_1 region but shows damped oscillatory behavior in the F_2 layer and eventually vanishes in the S region. However, S_x is a constant throughout the F_2 and S regions and oscillates in F_1 layers. We found that S_y (the component normal to the layers) depends very weakly on the bias, and thus its spatial dependence arises largely from a static effect. The bias dependence of S_x in the S region is very similar to that of the tunneling charge current in normal/superconductor systems with high barriers: S_x vanishes in the subgap regions and arises right above the gap. The behavior of **m** is consistent with that of **S**. We found that m_x, parallel to the local exchange fields in F_2, spreads out over the S regions when the bias is larger than the superconducting gap. We have also investigated the bias dependence of the spin transfer torques, and we have carefully verified that the appropriate continuity equation for the spin current is strictly obeyed in our self-consistent approach. Our method can be extended to include the effects of interfacial scattering and wavevector mismatch. It can also be used for further study of the intricate phenomena associated with spin transport in these systems.

ACKNOWLEDGMENTS

Portions of this work were supported by IARPA grant No. N66001-12-1-2023. CTW thanks the University of Minnesota for a Dissertation Fellowship. The authors thank I. Krivorotov (Irvine) for helpful discussions.

* wu@physics.umn.edu
† otvalls@umn.edu; Also at Minnesota Supercomputer Institute, University of Minnesota, Minneapolis, Minnesota 55455
‡ klaus.halterman@navy.mil

[1] I. Žutić, J. Fabian, and S. Das Sarma, Rev. Mod. Phys.**76**, 323 (2004).
[2] A. I. Buzdin, Rev. Mod. Phys. **77**, 935 (2005).
[3] E. A. Demler, G. B. Arnold, and M. R. Beasley, Phys. Rev. B**55**, 15174 (1997).
[4] K. Halterman and O. T. Valls, Phys. Rev. B**65**, 014509 (2001).
[5] K. Halterman and O. T. Valls, Phys. Rev. B**66**, 224516 (2002).
[6] Buzdin, A. I., and M. Y. Kuprianov, Pisma Zh. Eksp. Teor. Phys. **52**, 1089-1091 [JETP Lett. **52**, 487-491 (1990)].
[7] K. Halterman and O. T. Valls, Phys. Rev. B**70**, 104516 (2004).
[8] A. F. Andreev, Sov. Phys. JETP **19**, 1228 (1964).
[9] G. E. Blonder, M. Tinkham, and T. M. Klapwijk, Phys. Rev. B**25**, 4515 (1982).
[10] S. Kashiwaya, Y. Tanaka, M. Koyanagi, and K. Kajimura, Phys. Rev. B**53**, 2667 (1996).
[11] M. J. M. de Jong and C. W. J. Beenakker, Phys. Rev. Lett.**74**, 1657 (1995).
[12] I. Žutić and O. T. Valls, Phys. Rev. B**60**, 6320 (1999).
[13] I. Žutić and O. T. Valls, Phys. Rev. B**61**, 1555 (2000).
[14] I. I. Mazin, Phys. Rev. Lett.**83**, 1427 (1999).
[15] R. J. Soulen Jr., J. M. Byers, M. S. Osofsky, B. Nadgorny, T. Ambrose, S. F. Cheng, P. R. Broussard, C. T. Tanaka, J. Nowak, J. S. Moodera, A. Barry, and J. M. D. Coey, Science **282**, (5386):85-88 (1998).
[16] S. K. Upadhyay, A. Palanisami, R. N. Louie, and R. A. Buhrman, Phys. Rev. Lett.**81**, 3247 (1998).
[17] P. Raychaudhuri, A. P. Mackenzie, J. W. Reiner, and M. R. Beasley, Phys. Rev. B**67**, 020411 (2003).
[18] P. Chalsani, S. K. Upadhyay, O. Ozatay, and R. A. Buhrman, Phys. Rev. B**75**, 094417 (2007).
[19] S. Hacohen-Gourgy, B. Almog, and G. Deutscher, Appl. Phys. Lett. 92, 152502 (2008).
[20] F.S. Bergeret, A.F Volkov, and K.B. Efetov, Phys. Rev. Lett.**86**, 3140 (2001); Phys. Rev. B**68**, 064513 (2003); Rev. Mod. Phys. **77**, 1321-1373 (2005).
[21] F. S. Bergeret, A. F. Volkov, and K. B. Efetov, Appl. Phys. A **89**, 599 (2007)
[22] J. Wang, M. Singh, M. Tian, N. Kumar, B. Liu, C. Shi, J. K. Jain, N. Samarth, T. E. Mallouk, and M. H. W. Chan, Nat. Phys. **6**, 389 (2010).
[23] F. Hübler, M. J. Wolf, T. Scherer, D. Wang, D. Beckmann, and H. v. Löhneysen, Phys. Rev. Lett.**109**, 087004 (2012).
[24] K. Halterman, O. T. Valls, and P. H. Barsic, Phys. Rev. B**77**, 174511 (2008).
[25] R. S. Keizer, S. T. B. Goennenwein, T. M. Klapwijk, G. Miao, G. Xiao, and A. Gupta, Nature **439**, 825 (2006).
[26] J. W. A. Robinson, J. D. S. Witt, and M. G. Blamire, Science **329**, 59 (2010)
[27] T. S. Khaire, M. A. Khasawneh, W. P. Pratt, Jr., and N. O. Birge, Phys. Rev. Lett.**104**, 137002 (2010).
[28] K. Halterman and O. T. Valls, Phys. Rev. B**80**, 104502 (2009).
[29] M. Eschrig and T. Löfwander, Nature Physics **4**, 138 (2008).
[30] K. Halterman, P. H. Barsic, and O. T. Valls, Phys. Rev. Lett.**99**, 127002 (2007).
[31] J. Linder, T. Yokoyama, and A. Sudbø, Phys. Rev. B**79**, 224504 (2009).
[32] C. Visani, Z. Sefrioui, J. Tornos, C. Leon, J. Briatico, M. Bibes, A. Barthélémy, J. Santamaría, and Javier E. Villegas, Nature Phys. **8**, 539 (2012).
[33] Z. P. Niu, Europhys. Lett. **100** 17012 (2012).
[34] Y.-Q. Ji, Z.-P. Niu, C.-D. Feng, and D.-Y. Xing, Chinese Phys. Lett. **25**, 691 (2008)
[35] C. D. Feng, Z. M. Zheng, R. Shen, B. Wang, and D. Y. Xing, Phys. Rev. B**81**, 224510 (2010)
[36] A. A. Jara, C. Safranski, I. N. Krivorotov, C.-T. Wu. A. N. Malmi-Kakkada, O. T. Valls, and K. Halterman, Phys. Rev. B**89**, 184502 (2014).
[37] P.V. Leksin, N. N. Garif'yanov, I. A. Garifullin, Ya.V. Fominov, J. Schumann, Y. Krupskaya, V. Kataev, O. G. Schmidt, and B. Büchner, Phys. Rev. Lett.**109**, 057005 (2012).
[38] V. I. Zdravkov, J. Kehrle, G. Obermeier, D. Lenk, H.-A. Krug von Nidda, C. Müller, M. Yu. Kupriyanov, A. S. Sidorenko, S. Horn, R. Tidecks , and L. R. Tagirov, Phys. Rev. B**87**, 144507 (2013).

[39] C.-T. Wu, K. Halterman, and O. T. Valls, Phys. Rev. B**86**, 014523 (2012).
[40] Q. Cheng and B. Jin, Physica C: Superconductivity **473**, 29 (2012).
[41] S. Kashiwaya, Y. Tanaka, N. Yoshida, and M. R. Beasley, Phys. Rev. B**60**, 3572 (1999).
[42] T. Yamashita, S. Takahashi, H. Imamura, and S. Maekawa, Phys. Rev. B**65**, 172509 (2002).
[43] L. Berger, Phys. Rev. B**54**, 9353 (1996).
[44] E. B. Myers, D. C. Ralph, J. A. Katine, R. N. Louie, and R. A. Buhrman, Science **285**, 867 (1999).
[45] M. Bozŏvić and Z. Radović, Phys. Rev. B**66**, 134524 (2002).
[46] F. Romeo and R. Citro, Phys. Rev. B**84**, 024531 (2011).
[47] J. Linder and A. Sudbø, Phys. Rev. B**75**, 134509 (2007).
[48] R. Grein, T. Löfwander, G. Metalidis, and M. Eschrig, Phys. Rev. B**81**, 094508 (2008).
[49] P. H. Barsic and O. T. Valls Phys. Rev. B**79**, 014502 (2009).
[50] P. G. de Gennes, *Superconductivity of Metals and Alloys* (Addison-Wesley, Reading, MA, 1989).
[51] A. Spuntarelli, P. Pieri, and G. C. Strinati, Physics Reports **488**, 111 (2010).
[52] J.-X. Zhu, C.S. Ting, Phys. Rev. B**61**, 1456 (2000).
[53] G. Baym and L.P. Kadanoff, Phys. Rev. **124**, 287 (1961).
[54] With a current present, one cannot adopt the expedient of choosing real wavefunctions.
[55] P.F. Bagwell, Phys. Rev. B**49**, 6841 (1993).
[56] F. Sols and J. Ferrer, Phys. Rev. B**49**, 15913 (1994).
[57] J. Sanchez-Canizares and F. Sols, Phys. Rev. B**55**, 531 (1997).
[58] Y.V. Fominov, A.A. Golubov, T.Y. Karminskaya, M.Y. Kupriyanov, R.G. Deminov, and L.R. Tagirov, JETP Letters **91**, 308 (2010).
[59] S. Oh, D. Youm, and M. R. Beasley, Appl. Phys. Lett. **71**, 2376 (1997).
[60] M. Eschrig, J. Kopu, J. C. Cuevas, and G. Schrön, Phys. Rev. Lett.**90**, 137003 (2003).
[61] J. Linder, M. Cuocco, and Asle Sudbø, Phys. Rev. B**81**, 174526 (2010).
[62] D.C. Ralph and M.D. Stiles, J. Magn, Magn. Mater. **320**, 1190 (2008).